RIPK1 Biallelic Activating Variants lead to Autoinflammatory Disease Driven by T cell Death

Jialin Dai[1,3,11], Taijie Jin[2,3,11], Gaixiu Su[4,11], Xu Han[3], Jun Wang[3], Chenlu Liu[3], Wenjie Zheng[5], Qiuye Zhang[6], Jun Yang[7], Li Guo[8], Dan Zhang[4], Ming Li[4], Yingjie Xu[4], Tong Yue[4], Min Wen[4], Jia Zhu[4], Min Kang[4], Jianming Lai[4], Feifei Wu[4], Shihao Wang[3], Jiahui Zhang[3], Pui Y. Lee[9], Junying Yuan[10]*, Xiaomin Yu[1,2]*, Qing Zhou[1,3]*

1 Liangzhu Laboratory of Zhejiang University, and Department of Rheumatology, Sir Run Run Shaw Hospital, Zhejiang University School of Medicine, Hangzhou, Zhejiang, China

2 Department of Rheumatology, The Second Affiliated Hospital, Zhejiang University School of Medicine, Hangzhou, Zhejiang, China

3 Life Sciences Institute, Zhejiang University, Hangzhou, Zhejiang, China

4 Department of Rheumatology and Immunology, Capital Institute of Pediatrics, Beijing, China

5 The Second Affiliated Hospital and Yuying Children's Hospital of Wenzhou Medical University, Wenzhou, Zhejiang, China

6 Department of Pediatric Nephrology, Rheumatology and Immunity, The Affiliated Hospital of Qingdao University, Qingdao, China

7 Department of Rheumatology and Immunology, Shenzhen Children's hospital, Shenzhen, China

8 Department of Rheumatology Immunology & Allergy, Children's Hospital, Zhejiang University School of Medicine, Hangzhou

9 Division of Immunology, Boston Children's Hospital, Harvard Medical School, Boston, MA, USA

10 Interdisciplinary Research Center on Biology and Chemistry, Shanghai Institute of Organic Chemistry, Chinese Academy of Sciences, Shanghai, China

11 These authors contributed equally: Jialin Dai, Taijie Jin, Gaixiu Su.

*These authors jointly supervised this work: Qing Zhou, Xiaomin Yu, Junying Yuan.

Corresponding authors

*E-mail: zhouqingnwu@gmail.com; yuxiaomin78@gmail.com; junying_yuan@sioc.ac.cn.

Abstract

Receptor-interacting serine/threonine-protein kinase 1 (RIPK1) is a key regulator of cell fate decision between pro-survival signaling and programmed cell death. The activation of RIPK1 is extensively modulated by posttranslational modification, such as ubiquitination. RIPK1 overactivation mediates autoinflammatory diseases in humans. However, the role of RIPK1 ubiquitination in human autoinflammatory diseases has not been reported, and the mechanism mediating the interaction of cell death and autoinflammation is largely unknown. Here, we report two patients carrying compound heterozygous *RIPK1* variants K377E/R390G with recurrent fevers, lymphadenopathy and skin rashes. Mechanistically, K377E and R390G mutations impaired ubiquitination of RIPK1, which suppresses the formation of TNFR1 signaling complex (TNF-RSC) and NF-κB activation, resulting in the loss of $CD8^+$ T cells mediated by RIPK1 activation-induced cell death in the patients. We reveal that the death of $CD8^+$ T cells promotes the secretion of TNF and IFNγ to activate monocytes and macrophages, which triggers further production of proinflammatory cytokines to amplify autoinflammation. Disruption of the communication between T cells and monocytes/macrophages through pharmacologic blockade of TNF and IFNγ attenuated proinflammatory cytokine production in macrophages. Collectively, our results demonstrate a crucial role of RIPK1 ubiquitination in regulating $CD8^+$ T cell death and restraining autoinflammation. Our study demonstrates the mechanism for a group of autoinflammatory diseases mediated by RIPK1 activation-induced cell death, and highlights an important role of $CD8^+$ T cells in driving autoinflammation.

50 **Introduction**

51 Systemic autoinflammatory diseases (SAIDs) are a group of disorders induced by overactivation of
52 innate immune system characterized by recurrent fever and multi-organ inflammation, but typically
53 without high-titer antibodies or antigen-specific T cells. Distinct from autoimmune diseases defined by
54 dysregulation of the adaptive immune system, SAIDs are believed to be mostly driven by the malfunction
55 of innate immune cells such as monocytes and neutrophils [1,2]. Therefore, the contribution of adaptive
56 immune cells in triggering activation of myeloid cells has not been appreciated in the pathogenesis of
57 SAIDs.

58 To date, more than 50 genes responsible for monogenic SAIDs have been identified. The list of
59 genes whose mutations lead to SAIDs are enriched with key regulators of programmed cell death (PCD).
60 Enhanced PCD is one of the characteristics in the SAID patients caused by the cleavage resistance
61 mutations in *RIPK1*[3-5] or deficiencies of *RIPK1*[6,7], TANK-binding kinase 1 (*TBK1*)[8], OTU deubiquitinase
62 with linear linkage specificity (*OTULIN*), HOIL1-interacting protein (*HOIP*), Heme-oxidized IRP2
63 ubiquitin ligase-1 (*HOIL1*) and Shank-associated RH domain-interacting protein (*SHARPIN)*[9].
64 Pathogenic variants of these genes have been shown to activate apoptosis and necroptosis in cellular or
65 murine models[10]. While excessive cell death is strongly linked to autoinflammatory diseases in humans,
66 the mechanism by which cell death causes spontaneous inflammation in these conditions is unknown.

67 RIPK1 is a key mediator of cell death and inflammation[11]. Overactivation of RIPK1 leads to
68 enhanced apoptosis, necroptosis and inflammatory response in mice and humans[12]. Whereas *RIPK1*
69 deficiency and heterozygous non-cleavable variants in *RIPK1* cause immunodeficiency and dominantly
70 inherited autoinflammatory diseases, respectively, a recessive autoinflammatory disease caused by
71 *RIPK1* variants has not been reported. K63-linked ubiquitination of RIPK1 on K377 is essential for NF-
72 κB pathway activation and negative regulation of cell death. Mice bearing *Ripk1*$^{K376R/K376R}$ knockin
73 mutation displays embryonic lethality due to excessive apoptosis and necroptosis caused by RIPK1
74 activation[13-15]. Ablation of *Fadd* and *Mlkl/Ripk3* rescues the embryonic lethality and allows them to grow
75 into fertile adults. Nevertheless, the function of RIPK1 ubiquitination in human disease has not been
76 defined and studied. In this study, we identified two autoinflammatory patients carrying recessively
77 inherited compound heterozygous *RIPK1* variants K377E/R390G. We demonstrate that *RIPK1*
78 K377E/R390G variants lead to autoinflammatory disease by prompting RIPK1 activation-mediated the
79 death of $CD8^+$ T cells.

Results

Biallelic *RIPK1* mutations in patients with autoinflammation

We identified two children from one family with autoinflammatory disease characterized by recurrent fevers, lymphadenopathy and skin rashes (Fig. 1a-d). The proband (Patient 1, P1) exhibited very early onset inflammatory bowel disease (VEO-IBD) characterized by diarrhea, abdominal pain and perianal abscess. At the age between 0-5, respectively, P1 and patient 2 (P2) displayed fever episodes that last 3-4 days and recurred every 8-9 days. Their fever episodes were accompanied by elevated serum C-reactive protein (CRP), serum amyloid A (SAA), erythrocyte sedimentation rate (ESR), D-dimer and lactate dehydrogenase (LDH) (Fig. 1e, Extended Data Fig. 1a-c). Neither case exhibited evidence of immunodeficiency or infection. In addition, the levels of pro-inflammatory cytokines IL-6 and TNF were strongly increased in the serum of both patients during flares (Fig. 1f). Serum CRP levels and adenosine deaminase (ADA) activity in patients were higher than that of unaffected controls and parents during disease flares and even in remission (Fig. 1f). P1 had taken prednisone during flares, with resolution of fever but limited effect on inflammatory indexes (Fig. 1e, Extended Data Fig. 1a-c).

By performing whole exome sequencing (WES) and sanger sequencing on the family, we identified that both P1 and P2 carried the *RIPK1* compound heterozygous mutations (c. 1129A>G / p. K377E and c. 1168C>G / p. R390G), whereas their unaffected mother and father were heterozygous carriers of *RIPK1* R390G and K377E, respectively (Fig. 1g, Extended Data Fig. 1d-e). Therefore, this autoinflammatory disease in the siblings appeared to be recessively inherited and segregated with the inheritance of both *RIPK1* variants. The lysine residue at amino acid position 377 is the site for K63-linked ubiquitination of RIPK1[16], while the function of residue R390 has not been characterized. Both K377 and R390 residues are conserved in RIPK1 across species (Fig. 1h). The two *RIPK1* variants were predicted to be deleterious with their CADD scores well above that of the non-cleavable *RIPK1* mutations D324V, D324H and D324N (Extended Data Fig. 1f).

RIPK1 activating mutations impair ubiquitination of RIPK1 and NF-κB activation and promote cell death

Given that RIPK1 is a widely expressed regulator of pro-survival NF-κB signaling and programmed cell death, we utilized SV40-immortalized human dermal fibroblasts (SV40-HDFs) derived from unaffected controls and P2 to assess the functional status of these signaling pathways. SV40-HDFs from P2 show

110 increased sensitivity to apoptosis induced by TNF (T) with cIAP1/2 degrader SM-164 (S) as well as
111 necroptosis induced by TNF (T) with pan-caspase inhibitor z-VAD-FMK (Z) or TSZ (Fig. 1i, Extended
112 Data Fig. 2a), and enhanced RIPK1 activation as shown by phosphorylation at S166 and that of MLKL
113 as shown by phosphorylation at S358, which were rescued by the RIPK1 kinase inhibitor Necrostatin-1s
114 (Nec-1s) (Fig. 1j, Extended Data Fig. 2a). These results suggest that the compound R390G and K377E
115 mutations in RIPK1 promote the activation of RIPK1.

116 TNF-RSC is an important signaling complex that forms within minutes upon TNFR1 activation by
117 TNF[17]. We next determined the effect of R390G and K377E compound mutations on TNF-RSC
118 formation in SV40-HDFs upon stimulation with Flag-TNF. Ubiquitination of RIPK1 as well as
119 recruitment of NEMO, IKKβ and SHARPIN to the TNF-RSC were impaired in P2 SV40-HDFs
120 compared to unaffected controls (Fig. 1k). Furthermore, the activation of NF-κB and MAPK signaling
121 by TNF were impaired in P2 SV40-HDFs as revealed by reduced phosphorylation of IKKα/β, p65, IκBα,
122 ERK and JNK (Fig. 1l).

123 The above findings were further investigated in *RIPK1*$^{-/-}$ HT-29 cell lines complemented with wild-
124 type (WT), K377E and R390G RIPK1. K377E and R390G compound mutations sensitized HT-29 cells
125 to RIPK1-dependent cell death (Extended Data Fig. 2b-c). Furthermore, *RIPK1*$^{-/-}$ HT-29 cells expressed
126 K377E or R390G RIPK1 alone were also sensitized to TS and TSZ stimulation induced cell death to the
127 same extent as that express both K377E and R390G (Fig. 1m-n, Extended Data Fig. 2d). Thus, K377E
128 and R390G compound mutations or single mutation alone can promote cell death. Notably, the
129 expression of K377E and R390G compound mutations or individual K377E and R390G mutation alone
130 also reduced the levels of RIPK1 ubiquitination in TNF-RSC (Fig. 1o), as well as the activation of NF-
131 κB and MAPK (Fig. 1p), and the production of downstream cytokines (Extended Data Fig. 2e).
132 K377 is a ubiquitination site in RIPK1 intermediate domain (ID domain)[16]. Consistently, K377E, but not
133 R390G, directly abolished the ubiquitination of ID domain (Extended Data Fig. 2f). Since R390 is not
134 expected to be the site of ubiquitination, we considered the possibility that R390G might affect the
135 recruitment of E3 ubiquitination complexes. Mind Bomb-2 (MIB2) is known to be an E3 ubiquitin ligase
136 recruited to TNF-RSC to mediate RIPK1 ubiquitination[18]. We found that the interaction between Mind
137 Bomb-2 (MIB2) and RIPK1 R390G was demonstrated to be significantly reduced, which partly
138 explained for the impaired ubiquitination of R390G RIPK1 (Extended Data Fig. 2g). Collectively, these
139 data demonstrate that both K377E and R390G mutations promote RIPK1 activation-dependent cell death

140 and impaired pro-survival NF-κB signaling by modulating RIPK1 ubiquitination in TNF-RSC.

141

142 **Activation of inflammatory signaling in myeloid cells of the patients**

143 We next studied the inflammatory signaling pathways by performing single-cell RNA sequencing on
144 peripheral blood mononuclear cells (PBMCs) from P1, P2 and three unaffected controls. The monocyte
145 compartment in patients was significant expanded (Fig. 2a, Extended Data Fig. 3a). Similar to the
146 previously reported *RIPK1* D324V mutant[4], transcriptional up-regulation of proinflammatory cytokines
147 (*IL1B* and *CXCL8*) was detected in patient cells, especially in monocyte subsets (Fig. 2b). Likewise,
148 differential gene expression analysis revealed greatest up-regulation of genes governed by NF-κB and
149 type-I IFN pathways in myeloid cells from the patients (Fig. 2c-d, Extended Data Fig. 3b-c). The up-
150 regulated genes in the patients' monocytes were also enriched for pathways of cytokine production,
151 cytokine stimulation, and negative regulation of cell death in the gene ontology (GO) analysis (Fig. 2e,
152 Extended Data Fig. 3d), suggesting that myeloid cells play a crucial role in increased cytokine production
153 and pro-inflammatory signal transduction in the patients. Increased basal expression of IL-1β, IL-6 as
154 well as IFNγ in monocytes from P1 was confirmed by flow cytometry (Fig. 2f). However, monocytes
155 isolated from the patients exhibited reduced transcription of NF-κB regulated genes including *IL1B*, *IL6*,
156 *CXCL8* and *TNF* in response to TNF stimulation (Fig. 2g), in accordance with suppressed NF-κB
157 activation in SV40-HDFs as demonstrated earlier (Fig. 1k, l). Thus, the increased inflammatory response
158 of myeloid cells in the patients was likely represented a secondary effect triggered by K377E/R390G
159 variants.

160 As RIPK1 overactivation can promote programmed cell death leading to inflammation[19], we
161 assessed the cell death response of monocytes to TNF stimulation. The monocytes from the patients were
162 more sensitive to TS-induced apoptosis than that of unaffected controls, whereas they showed similar
163 sensitivity to necroptosis induced by TSZ (Fig. 2h). In addition, no differences of apoptosis and
164 necroptosis were observed between monocyte-derived macrophages (MDMs) from patients and that
165 from unaffected controls (Fig. 2i, Extended Data Fig. 3e). On the other hand, although the expression of
166 cell death suppressor genes *TNFAIP3*, *BCL2A1*, *BCL6*, *BCL3*, *RNF144B*, *BIRC2* and *BIRC3* were
167 elevated in patients' various immune cell types, monocytes, LDG and DC cells express these genes
168 significantly higher than that in lymphocyte subsets (Fig. 2j, k and Extended Data Fig. 3f). These results
169 suggest that the elevated inflammatory response of monocytes induced by K377E/R390G variants may

170 be regulated non-autonomously by other cell types that were more susceptible to cell death.

171 To define the upstream factors that drove the overproduction of inflammatory cytokines in
172 monocytes, we employed semi-quantitative protein microarray analysis on serum samples from
173 unaffected controls and P2 (Fig. 2l-m). We collected samples before and after the first fever episode
174 (disease onset) for P2. Differentially expressed cytokines were clustered into three groups according to
175 the data trend. Twenty-eight cytokines in group 1 (such as IL-1β) peaked during flare, reflecting a direct
176 correlation with fever status (Fig. 2n, Extended Data Fig. 4a-b). 24 cytokines in group 2 (such as sCD95)
177 (Fig. 2n, Extended Data Fig. 4c-d) and 32 cytokines in group 3 (Extended Data Fig. 4e-f) continuously
178 changed across samples of P2. Up-regulated cytokines in group 2 were considered to be directly regulated
179 by the *RIPK1* K377E/R390G mutations.

180 To further define the source of the cytokines in group 1 and 2, we compared the expression scores
181 of the two groups between patients and unaffected controls by analyzing single cell RNA-seq data. The
182 cytokines in group 1 were most significantly up-regulated in patients' monocytes, low-density
183 granulocyte (LDG), plasmacytoid dendritic cell (pDC) and plasma cells (Fig. 2o), consistent with the
184 strong inflammatory signature in myeloid cells during fever. Notably, the genes encoding cytokines in
185 group 2 were up-regulated most significantly in the patients' lymphocyte subsets, especially in $CD8^+$ T
186 cells (Fig. 2o), implying a pathogenic role of K377E/R390G variants in T lymphocytes. In addition, the
187 expression levels of cell death suppressor genes in T lymphocytes were also lower compared with
188 monocytes, LDG, pDC and plasma cells (Extended Data Fig. 3f), suggesting that T lymphocytes may be
189 sensitized to undergo programmed cell death. Collectively, these results supported a critical role of
190 monocytes in promoting inflammation and implied that T lymphocyte subsets may also contribute to the
191 pathophysiology of this autoinflammatory disease.

192

193 **RIPK1 activation leads to increased cell death and CD4/CD8 ratio in T cells**

194 To better understand the impact of *RIPK1* mutations on immune profile, we performed cytometry by
195 time-of-flight (CyTOF) on PBMCs isolated from unaffected controls and patients. CyTOF result revealed
196 that $CD4^+$T, B and γδ T cell proportions in patients were elevated whereas $CD8^+$ T and NK cell
197 proportions were reduced comparing to unaffected controls (Extended Data Fig. 5a-b). Apoptosis
198 indicated by cleaved caspase-3 was increased in $CD8^+$ TEMRA, γδT, NK and B cell subsets of patients
199 (Fig. 3a). Flow cytometric analysis confirmed that patients' $CD4^+$ and $CD8^+$ T cells, not $CD19^+$ B cells

200 and CD14$^+$ monocytes, displayed augmented activation of RIPK1 and cleaved caspase-3 (Fig. 3b-e,
201 Extended Data Fig. 5c-f). Furthermore, CD3$^+$ T cells isolated from patients were more sensitive to TS-
202 induced apoptosis and TSZ-induced necroptosis. They displayed higher levels of RIPK1 phosphorylation
203 at S166 and MLKL phosphorylation at S358 comparing to that of unaffected controls, and these patterns
204 were inhibited by treatment with Nec-1s (Fig. 3f-g), indicating that T cells bearing K377E/R390G
205 mutations were more prone to RIPK1-dependent cell death. In accordance with the recessive inheritance,
206 no significant differences of cell death were observed between unaffected parents carrying heterozygous
207 mutation and unaffected controls.

208 The CyTOF results also revealed a global activation of patients' immune cells as indicated by CD69
209 expression, while elevated CD38 expression appeared to be restricted to B cells and T cells (Extended
210 Data Fig. 5g-h). Increased expression of CD69 in T cells was further validated by flow cytometry (Fig.
211 3h). Concomitantly, higher levels of T cell activation-related proinflammatory mediators including
212 sCD25, TNF and IFNγ were observed in the serum of P1 and P2 as well as (cleavage-resistant RIPK1-
213 induced autoinflammatory) CRIA patients (Fig. 3i). Activated lymphocytes undergo cell expansion and
214 indeed we observed an elevation in the number of total lymphocytes, as well as that of CD3$^+$ T cells,
215 CD4$^+$ T cells and B cells, except for that of cytotoxic CD8$^+$ T cells and NKT cells in the
216 immunophenotyping results (Fig. 3j, Extended Data Fig. 6a). As a consequence of the loss of CD8$^+$ T
217 cells, CD4/CD8 ratio was significantly increased in patients. *In vitro* expansion of T cells isolated from
218 patients upon anti-CD3/CD28 stimulation were abnormal, but the proliferation ability was undampened
219 (Fig. 3k-l), reflecting the occurrence of T cell death. Specifically, CD8$^+$ T cells went through a contraction
220 phase after activation presumably resulted from activation-induced cell death (AICD) [20]. The augmented
221 signal of CD95 (Fas) on the surface of patients' T cells accompanied by elevations of serum sCD95 and
222 CD95L levels also supported increased AICD (Fig. 3i, m).

223 To further characterize the abnormalities in the patient T cells, we analyzed T cell subsets from *in*
224 *vitro* cultured PBMCs. We observed that CD8 expression was decreased in approximate half of the CD8$^+$
225 T cells after culturing PBMCs isolated from P2 *in vitro* for 24 hours, while the expression on CD8$^+$ T
226 cells of unaffected controls remained normal (Fig. 3n). Through gating on CD8^{hi} (CD8$^+$ T cells with
227 normal CD8 expression) or CD8^{lo} (CD8$^+$ T cells with lower CD8 expression) T cells, we found that in
228 contrast to CD8^{hi} T cells, most of the CD8^{lo} T cells exhibited augmented cleaved caspase-3 (Fig. 3n),
229 indicative of activated apoptosis. In addition, total RIPK1 level in CD8^{lo} T cells decreased which may be

230 caused by caspase-3 cleavage (Fig. 3n). The decreased CD8 expression in patients' T cells and the
231 increases in CD4/CD8 ratio were more prominent after prolonged *in vitro* culture and after TS or TSZ
232 stimulation compared to that of control (Fig. 3o, Extended Data Fig. 6b-d). The elevation of CD4/CD8
233 ratio induced by TS or TSZ could be inhibited by RIPK1 kinase inhibitor or *in situ* knockin of WT *RIPK1*
234 (Fig. 3p-q, Extended Data Fig. 6e-f). In contrast, neither ferroptosis induced by RSL3 nor RIPK1-
235 independent apoptosis induced by staurosporine (STS) can differentiate cell death of $CD8^+$ T cells from
236 the patients compared to that of unaffected controls (Extended Data Fig. 6g). In addition, the activation
237 of patients' T cells by anti-CD3 antibody stimulation increased CD4/CD8 ratio, which could be reversed
238 by ponatinib or partially reversed by Nec-1s (Fig. 3r-t). Since ponatinib inhibits the kinase activity of
239 RIPK1 and RIPK3 [21], these results suggest that they might play important roles in regulating AICD in
240 the patient T cells bearing K377E/R390G compound RIPK1 mutations. Together, these results suggested
241 that T cells, especially $CD8^+$ T cells, were the most susceptible hematopoietic lineage to RIPK1-mediated
242 cell death in patients with the *RIPK1* K377E/R390G variants.
243
244 **RIPK1 activation-induced T cell death drives inflammation in myeloid cells**
245 Given the differential impact of the *RIPK1* K377E/R390G variants on T cells and monocytes, we next
246 investigated cell-cell communication between these two cell types using a transwell system (Fig. 4a).
247 The results showed that patients' T cells induced higher cytokine expression in MDMs comparing to that
248 of T cells isolated from unaffected controls (Fig. 4b, c). However, MDMs from patients showed less
249 response than that of unaffected controls upon culturing with the identical T cells. The impaired
250 inflammatory response by patients' MDMs may be explained by the suppressed NF-κB activation caused
251 by *RIPK1* K377E/R390G mutations. Interestingly, patients' T cells could still trigger massive cytokine
252 production in autologous MDMs (Extended Data Fig. 7a). Thus, we conclude that increased cell death
253 by T cells from the patients can act to potentiate the inflammatory response of monocytes and
254 macrophages with *RIPK1* K377E/R390G mutations.
255 Previous studies have proposed TNF and IFNγ secreted by chimeric antigen receptor (CAR) T cells
256 as key contributors to the activation of macrophage during cytokine release syndrome (CRS) [22]. TNF
257 combined with IFNγ were also reported to be a key inducer of inflammation in patients with severe
258 COVID-19 [23]. Intriguingly, IFNγ and TNF were specifically upregulated in patients' T lymphocytes and
259 NK cells whereas receptors of these two cytokines were highly expressed in myeloid cells (Fig. 4d,

260 Extended Data Fig. 7b, c), providing additional support for T cell-monocyte/macrophage communication
261 through these two receptor-ligand pairs. In comparison to unaffected controls, T cells, especially $CD8^+$
262 T cells from patients, exhibited greater production of IFNγ and TNF. The production of these cytokines
263 was further enhanced upon TS or TSZ stimulation (Fig. 4e, Extended Data Fig. 7d). These results
264 indicated that IFNγ and TNF produced by activated T cells may be the key factors to initiate the
265 inflammatory response of MDMs. Consistently, increased production of *TNF*, *IL1B* and *IL6* in MDMs
266 generated from unaffected controls stimulated by either patient T cells or anti-CD3/CD28-activated
267 donor-matched T cells could be partially inhibited by neutralization of IFNγ or TNF alone. The cytokine
268 production was completely blocked by combined blockade of IFNγ and TNF (Fig. 4f, Extended Data
269 Fig. 7e). Collectively, these data demonstrated that RIPK1 overactivation in $CD8^+$ T cells promoted cell
270 death as well as TNF and IFNγ secretion to trigger inflammatory cytokine production in MDMs
271 (Extended Data Fig. 7f).

272 In order to validate this model and assess whether the function of *RIPK1* K377E and R390G
273 mutations in $CD8^+$ T cells was sufficient to induce inflammation, we exploited the Cre-loxp system
274 combined with bone marrow transplantation to conditionally express WT or mutated human RIPK1 in
275 specific hematopoietic compartments (Fig. 4g, Extended Data Fig. 8a). HSCs isolated from donor *Cd8a*-
276 creERT2 mice or *Lyz2*-creERT2 mice were transduced with lentivirus encoding *EF1α*-promoted *loxp-*
277 *GFP-stop-loxp-TagBFP2-P2A-human RIPK1* expression cassettes (*LSL-hRIPK1*). Afterwards,
278 transduced HSCs were transplanted into lethally irradiated donor mice followed by tamoxifen induction.
279 Transplantation efficiency and the specificities of *Cd8a* and *Lyz2* promoters were validated (Extended
280 Data Fig. 8b-h). GFP expression in HSCs reflected transduction efficiency, and TagBFP2 confirmed
281 WT/mutated RIPK1 expression in specific cell types upon tamoxifen induction (Extended Data Fig. 9a-
282 d). We then evaluated the serum levels of inflammatory cytokines in the recipients. Under basal
283 conditions, serum Tnf and Il-6 levels were higher in mice with $Cd8\alpha^+$ T cells expressing mutated RIPK1
284 (K377E, R390G or D324V) than WT RIPK1 and empty vector (EV) controls (Fig. 4h). No significant
285 differences were observed between mice bearing myeloid cells overexpressing EV/WT RIPK1 controls
286 and mutated RIPK1 (Fig. 4i). The result demonstrated the pathogenic function of K377E and R390G as
287 well as the initiator role of T cells in the autoinflammation. We also investigated the function of *RIPK1*
288 K377E/R390G mutations in myeloid cells. As TLR4 is specially highly expressed in myeloid cells, we
289 assessed the responsiveness of recipients to LPS at a nonlethal dose. The results showed that LPS

290 challenge led to elevation of Il-6 and Tnf in all groups. Recipients transplanted with HSCs expressing
291 mutated RIPK1 (K377E, R390G or D324V) under the control of *Lyz2*, but not *Cd8a* promoter displayed
292 higher serum level of inflammatory cytokines than WT and EV controls under LPS stimulation
293 (Extended Data Fig. 9e-f), which is consistent with myeloid-specific inactivation of TAK1 that caused
294 Ripk1 activation and cell death in mouse[24].

295 *RIPK1* mutations at D324 [3,4], which could activate RIPK1-dependent cell death, have been reported
296 to cause CRIA syndrome, respectively. Therefore, we examined the CD4/CD8 ratio and RIPK1 activation
297 in CRIA patients (CRIA-1 and CRIA-2) to verify our model. Similar to patients with *RIPK1*
298 K377E/R390G variants, we observed elevated CD4/CD8 ratio paired with increased RIPK1
299 phosphorylation and cleaved caspase-3 in PBMCs from CRIA patients (Fig. 4j-m, Extended Data Fig.
300 10a-b), indicating that $CD8^+$ T cell death might be a general phenomenon during the inflammation of
301 CRIA. Notably, *in vitro* culture also induced decreased CD8 expression in $CD8^+$ T cells of CRIA-1
302 (Extended Data Fig. 10c). CD4 and CD8 expression levels in CRIA patients' T cells were validated by
303 CyTOF and CD8 expression decreased more in $CD8^+$ TEMRA cells than other subsets, reflecting higher
304 levels of cell death in $CD8^+$ TEMRA cells (Extended Data Fig. 10d-g).

305

306 **Targeted therapies**

307 As TNF and IFNγ were considered to mediate the inflammatory cytokine production of myeloid cells,
308 we compared the treatment effectiveness of TNF inhibitor adalimumab with tocilizumab which blocks
309 the signaling of IL-6 mainly produced by myeloid cells in patients (Fig. 4n-o). Both P1 and P2 responded
310 to tocilizumab and showed marked alleviation of the elevated temperature and skin rashes and the
311 inflammatory indexes including abnormal CRP, WBC, neutrophil and lymphocyte. However, the serum
312 levels of TNF in both patients could not be suppressed by tocilizumab. TNF-targeting therapy is projected
313 to partially interrupt the communication between T cells and monocytes/macrophages in our model. P2
314 responded to anti-TNF therapy with reduced severity of the symptoms and decreased frequency of fevers.
315 However, adalimumab had limited effects on WBC and lymphocyte counts as well as symptoms of P1
316 as adalimumab alone was not enough to suppress serum levels of IL-6 (Fig. 4o), in accordance with the
317 partial inhibitory effect of adalimumab on IL-6 produced by MDMs in the co-culture assay.

318

319 **Discussion**

320 This is the first report of biallelic mutations K377E/R390G in *RIPK1* leading to early-onset SAIDs with
321 manifestations of periodic fever, intermittent lymphadenopathy, skin rashes and VEO-IBD. Mutation at
322 K377 blocks K63-linked ubiquitination of RIPK1, while function of *RIPK1* R390 has not been reported.
323 Here, we revealed that both K377E and R390G mutations lead to defects in TNF-RSC formation and
324 activation of RIPK1, which promote cell death and inflammation. Since K377E and R390G are the
325 recessive gain-of-function (GOF) mutations of *RIPK1*, as are the previously described caspase cleavage
326 resistance variants, we termed these two conditions as "Gain-of-function *RIPK1* variants-induced
327 autoinflammatory syndrome (GRIA)".

328 The condition in our study is inherited in an autosomal recessive (AR) pattern, which is different
329 from autosomal dominantly inherited CRIA syndrome even if they share similar manifestations.
330 Mutation in *RIPK1* D324 does not impair NF-κB pathway[3-5]; in contrast, compound heterozygous
331 mutations in *RIPK1* K377/R390 suppressed NF-κB activation, indicating that the autoinflammation
332 caused by these mutations is not directly induced by dysregulation of NF-κB. The evidence that PBMCs
333 and MEFs carrying heterozygous mutations in D324 as well as T cells carrying compound heterozygous
334 variants in *RIPK1* K377/R390 instead of heterozygous variant are hypersensitive to TNF-induced cell
335 death support the inheritance pattern of the two conditions[3,4]. Thus, excessive RIPK1-mediated cell death
336 triggered by heterozygous D324 mutations or biallelic K377E and R390G mutations is supposed to be
337 the inducer of autoinflammation. Mutations of genes such as *TBK1*[8], *OTULIN*, *HOIP*, *HOIL1* and
338 *SHARPIN*[9], haven been shown to cause several SAIDs. Variants of these genes have been studied in
339 murine models and are revealed to cause embryonic lethality attributed by enhanced cell death[17,25-27]. In
340 contrast, patients with programmed cell death-driven SAIDs (PCD-driven SAIDs) only manifest periodic
341 inflammation with excessive production of proinflammatory cytokines such as IL-6 and TNF.
342 Overactivation of cell death has been observed in the cells derived from these patients, supporting an
343 important role of cell death in the pathogenesis of SAIDs. However, how programmed cell death induces
344 autoinflammation in human diseases remains uninvestigated.

345 Our study provides a mechanism that K377E/R390G variants of *RIPK1* induce $CD8^+$ T cell death
346 to cause SAIDs. $CD8^+$ T cells bearing K377E/R390G have the propensity to be activated and expanded,
347 and then enter the contraction phase induced by programmed cell death. During this process, $CD8^+$ T
348 cells secret massive TNF and IFNγ which prime monocytes or macrophages to produce proinflammatory
349 cytokines. The accumulation of the inflammatory cytokines such as group 2 cytokines secreted from

350 monocytes would induce the onset of fever. At the same time, inflammation accelerates the proliferation
351 of T lymphocytes and autoinflammation with a positive feedback loop that amplifies the inflammatory
352 reaction (Extended Data Fig. 7f). Eventually, inflammation is terminated with the decrease of activated
353 $CD8^+$ T cells. Thus, we hypothesize that dynamics of CD4/CD8 ratio is correlated with the inflammatory
354 state. Consistently, we captured once the resting stage before T cell expansion of P2 as well as CRIA-2
355 with the normal ranges of WBC, lymphocyte counts and CD4/CD8 ratio. Therefore, increased CD4/CD8
356 ratio combined with augmented RIPK1 activation in T cells are supposed to be biomarkers for PCD-
357 driven inflammation. This evidence for diagnosis is verified in patients with CRIA syndrome. But it is
358 worth noting that intensive gating strategy is required as $CD8^{lo}$ T cells representing the dying $CD8^+$ T
359 cells may be considered as $CD8^+$ T cells by conventional gating strategy, leading to the falsely normal
360 CD4/CD8 ratio. Since RIPK1 activation-induced AICD of T cells trigger the inflammation in SAID
361 patients carrying *RIPK1* GOF variants, RIPK1 kinase inhibitors or RIPK1 proteolysis targeting chimeras
362 degraders may provide a promising strategy for the treatment of SAID induced by RIPK1
363 overactivation[11].

364 GRIA syndrome is characterized by selective cell death of $CD8^+$ T cells as reflected by the elevation
365 of CD4/CD8 ratio in peripheral lymphocytes. This process is remarkably similar to the contraction phase
366 of $CD8^+$ T cells following infections as most effector $CD8^+$ T cells undergo programmed cell death after
367 clonal expansion upon antigen-induced activation. Interestingly, intermittent fever with viremia has been
368 shown to be correlated with CD4/CD8 ratio, which is similar to high CD4/CD8 ratio in K377E/R390G
369 patients during flare[28]. Although the two diseases have completely different mechanism, it is worthwhile
370 to note that almost 14 days were needed for $CD8^+$ T cells to undergo expansion and contraction upon
371 antigen stimulation[29], which is identical to the period of intermittent fever in GRIA patients.

372 Taken together, our findings provide a new insight that not only innate immune system, but also
373 adaptive immune cells can play a causative role in the onset of SAIDs. We demonstrate that myeloid
374 cells, such as monocytes and macrophages, act as executors of PCD-driven SAIDs for that they take
375 responsibility to produce excessive cytokines to induce autoinflammation. This finding supports the
376 notion that SAIDs is induced by dysregulation of innate immune system. In addition, we also highlight
377 the essential role of T cells in PCD-driven SAIDs as they are the most sensitive hematopoietic
378 compartments to cell death and has the predisposition to undergo AICD which motivate inflammatory
379 response of myeloid cells, indicating the importance of cell-cell communication in pathogenesis of PCD-

driven SAIDs. Hence, blockade of communication between T cells and myeloid cells could be a promising therapeutic strategy for PCD-driven SAIDs.

Acknowledgements

We thank the patients, their families and the unaffected controls for their support during this research study. We also thank the core facility of the Life Sciences Institute, Zhejiang University, and core facilities of Liangzhu Laboratory, Zhejiang University. The works of Q.Z. were supported by grants 82225022, 32141004 and 32321002 from the National Natural Science Foundation of China. The works of X.Y. were supported by the Hundred-Talent Program of Zhejiang University. J.D. received grant 32300618 from the National Natural Science Foundation of China. J.W. received the grant 2023M733104 from China Postdoctoral Science Foundation. L.G. received the grant LHDMY23H100005 from Zhejiang Provincial Natural Science Foundation of China.

Author contributions

Q.Z., X.Y., and J.Y. directed and supervised the research. J.D., T.J., and G.S. contributed equally. J.D. and T.J. designed the study, performed experiments and analyzed most of the data. X.H., J.W., and C.L. analyzed data. S.W. and J.Z. performed experiments. G.S., W.Z., Q.Z., J.Y., P.Y.L., D.Z., M.L., Y.X., T.Y., M.W., J.Z., M.K., and J.L. enrolled the patients, collected and interpreted clinical information. J.D., T.J., Q.Z., J.Y., and P.Y.L. wrote the manuscript, with input from others. All authors contributed to the review and approval of the manuscript.

Competing interests

J.Y. is a consultant of Denali Therapeutics. The rest of authors declare no competing financial interests.

References

1 Manthiram, K., Zhou, Q., Aksentijevich, I. & Kastner, D. L. The monogenic autoinflammatory diseases define new pathways in human innate immunity and inflammation. *Nat Immunol* **18**, 832-842 (2017). https://doi.org:10.1038/ni.3777

2 Zhang, J., Lee, P. Y., Aksentijevich, I. & Zhou, Q. How to Build a Fire: The Genetics of Autoinflammatory Diseases. *Annu Rev Genet* (2023). https://doi.org:10.1146/annurev-genet-030123-084224

3 Lalaoui, N. *et al.* Mutations that prevent caspase cleavage of RIPK1 cause autoinflammatory

412 disease. *Nature* **577**, 103-108 (2020). https://doi.org:10.1038/s41586-019-1828-5
413 4 Tao, P. *et al.* A dominant autoinflammatory disease caused by non-cleavable variants of RIPK1.
414 *Nature* **577**, 109-114 (2020). https://doi.org:10.1038/s41586-019-1830-y
415 5 Tapiz, I. R. A. J. *et al.* Characterization of Novel Pathogenic Variants Leading to Caspase-8
416 Cleavage-Resistant RIPK1-Induced Autoinflammatory Syndrome. *J Clin Immunol* **42**, 1421-
417 1432 (2022). https://doi.org:10.1007/s10875-022-01298-2
418 6 Cuchet-Lourenco, D. *et al.* Biallelic RIPK1 mutations in humans cause severe
419 immunodeficiency, arthritis, and intestinal inflammation. *Science* **361**, 810-813 (2018).
420 https://doi.org:10.1126/science.aar2641
421 7 Li, Y. *et al.* Human RIPK1 deficiency causes combined immunodeficiency and inflammatory
422 bowel diseases. *Proc Natl Acad Sci U S A* **116**, 970-975 (2019).
423 https://doi.org:10.1073/pnas.1813582116
424 8 Taft, J. *et al.* Human TBK1 deficiency leads to autoinflammation driven by TNF-induced cell
425 death. *Cell* **184**, 4447-4463 e4420 (2021). https://doi.org:10.1016/j.cell.2021.07.026
426 9 Oda, H. *et al.* Human LUBAC deficiency leads to autoinflammation and immunodeficiency by
427 dysregulation in TNF-mediated cell death. *medRxiv*, 2022.2011.2009.22281431 (2022).
428 https://doi.org:10.1101/2022.11.09.22281431
429 10 Xu, D., Zou, C. & Yuan, J. Genetic Regulation of RIPK1 and Necroptosis. *Annu Rev Genet* **55**,
430 235-263 (2021). https://doi.org:10.1146/annurev-genet-071719-022748
431 11 Mifflin, L., Ofengeim, D. & Yuan, J. Receptor-interacting protein kinase 1 (RIPK1) as a
432 therapeutic target. *Nat Rev Drug Discov* **19**, 553-571 (2020). https://doi.org:10.1038/s41573-
433 020-0071-y
434 12 Degterev, A., Ofengeim, D. & Yuan, J. Targeting RIPK1 for the treatment of human diseases.
435 *Proc Natl Acad Sci U S A* **116**, 9714-9722 (2019). https://doi.org:10.1073/pnas.1901179116
436 13 Tang, Y. *et al.* K63-linked ubiquitination regulates RIPK1 kinase activity to prevent cell death
437 during embryogenesis and inflammation. *Nat Commun* **10**, 4157 (2019).
438 https://doi.org:10.1038/s41467-019-12033-8
439 14 Zhang, X. *et al.* Ubiquitination of RIPK1 suppresses programmed cell death by regulating
440 RIPK1 kinase activation during embryogenesis. *Nat Commun* **10**, 4158 (2019).
441 https://doi.org:10.1038/s41467-019-11839-w
442 15 Kist, M. *et al.* Impaired RIPK1 ubiquitination sensitizes mice to TNF toxicity and inflammatory
443 cell death. *Cell Death Differ* **28**, 985-1000 (2021). https://doi.org:10.1038/s41418-020-00629-
444 3
445 16 Ea, C. K., Deng, L., Xia, Z. P., Pineda, G. & Chen, Z. J. Activation of IKK by TNFalpha requires
446 site-specific ubiquitination of RIP1 and polyubiquitin binding by NEMO. *Mol Cell* **22**, 245-257
447 (2006). https://doi.org:10.1016/j.molcel.2006.03.026
448 17 Xu, D. *et al.* TBK1 Suppresses RIPK1-Driven Apoptosis and Inflammation during
449 Development and in Aging. *Cell* **174**, 1477-1491 e1419 (2018).
450 https://doi.org:10.1016/j.cell.2018.07.041
451 18 Feltham, R. *et al.* Mind Bomb Regulates Cell Death during TNF Signaling by Suppressing
452 RIPK1's Cytotoxic Potential. *Cell Rep* **23**, 470-484 (2018).
453 https://doi.org:10.1016/j.celrep.2018.03.054
454 19 Zhu, K. *et al.* Necroptosis promotes cell-autonomous activation of proinflammatory cytokine
455 gene expression. *Cell Death Dis* **9**, 500 (2018). https://doi.org:10.1038/s41419-018-0524-y

456 20 Badovinac, V. P., Porter, B. B. & Harty, J. T. Programmed contraction of CD8(+) T cells after
457 infection. *Nat Immunol* **3**, 619-626 (2002). https://doi.org:10.1038/ni804
458 21 Martens, S., Hofmans, S., Declercq, W., Augustyns, K. & Vandenabeele, P. Inhibitors Targeting
459 RIPK1/RIPK3: Old and New Drugs. *Trends Pharmacol Sci* **41**, 209-224 (2020).
460 https://doi.org:10.1016/j.tips.2020.01.002
461 22 Morris, E. C., Neelapu, S. S., Giavridis, T. & Sadelain, M. Cytokine release syndrome and
462 associated neurotoxicity in cancer immunotherapy. *Nat Rev Immunol* **22**, 85-96 (2022).
463 https://doi.org:10.1038/s41577-021-00547-6
464 23 Karki, R. *et al.* Synergism of TNF-alpha and IFN-gamma Triggers Inflammatory Cell Death,
465 Tissue Damage, and Mortality in SARS-CoV-2 Infection and Cytokine Shock Syndromes. *Cell*
466 **184**, 149-168 e117 (2021). https://doi.org:10.1016/j.cell.2020.11.025
467 24 Malireddi, R. K. S. *et al.* TAK1 restricts spontaneous NLRP3 activation and cell death to control
468 myeloid proliferation. *J Exp Med* **215**, 1023-1034 (2018).
469 https://doi.org:10.1084/jem.20171922
470 25 Kelliher, M. A. *et al.* The death domain kinase RIP mediates the TNF-induced NF-kappaB
471 signal. *Immunity* **8**, 297-303 (1998). https://doi.org:10.1016/s1074-7613(00)80535-x
472 26 Peltzer, N. *et al.* LUBAC is essential for embryogenesis by preventing cell death and enabling
473 haematopoiesis. *Nature* **557**, 112-117 (2018). https://doi.org:10.1038/s41586-018-0064-8
474 27 Bonnard, M. *et al.* Deficiency of T2K leads to apoptotic liver degeneration and impaired NF-
475 kappaB-dependent gene transcription. *EMBO J* **19**, 4976-4985 (2000).
476 https://doi.org:10.1093/emboj/19.18.4976
477 28 Murakami, K., Sentsui, H., Shibahara, T. & Yokoyama, T. Reduction of CD4+ and CD8+ T
478 lymphocytes during febrile periods in horses experimentally infected with equine infectious
479 anemia virus. *Vet Immunol Immunopathol* **67**, 131-140 (1999). https://doi.org:10.1016/s0165-
480 2427(98)00225-6
481 29 Prlic, M. & Bevan, M. J. Exploring regulatory mechanisms of CD8+ T cell contraction. *Proc*
482 *Natl Acad Sci U S A* **105**, 16689-16694 (2008). https://doi.org:10.1073/pnas.0808997105
483

484 **Methods**

485 **Patients**

486 Patients (P1 and P2; CRIA-1 and CRIA-2) were evaluated under protocols approved by Institutional
487 Review Board and Ethical Committee at the Children's Hospital of Zhejiang University School of
488 Medicine (protocol 2021-IRB-172). P1 and P2 were evaluated at Children's Hospital affiliated to the
489 Capital Institute of Pediatrics. All relevant ethical regulations were followed. All patients provided
490 written informed consent.

491

492 **Whole exome sequencing and genotyping with sanger sequencing**

493 Whole blood genomic DNA was extracted using Maxwell RSC Whole Blood DNA Kit (Promega,
494 AS1520) and 1 μg DNA was used for whole-exome sequencing. WES and data analysis were performed
495 as previously described[4]. For genotyping of other affected or unaffected family members, 437 bp
496 genomic DNA fragment containing *RIPK1* K377/R390 was amplified with forward primer 5'-TTGAGA
497 TACAGATTCATGACGGCG-3' and reverse primer 5'-CTGGTGCACTGCATTACCATGAC-3' for
498 sanger sequencing. For genotyping of CRIA patients, 514 bp genomic DNA fragment containing *RIPK1*
499 D324 was amplified with forward primer 5'-AAATCAGGAAGTGTGAGTCCTACAACC-3' and
500 reverse primer 5'-TGTTCAGAACACTCTATGACTGGTGAG-3' for sanger sequencing.

501

502 **Single-cell RNA sequencing**

503 PBMCs of patient 1 and patient 2 were freshly isolated and 10000 single-cell were captured by 10X
504 Genomics Chromium for cDNA library preparation according to the manufacturer's instruction.
505 Sequencing was carried out on Illumina NovaSeq PE150 platform by Novogene Company (Beijing,
506 China). The resulting count matrices followed the standard pipeline with default parameters. Further data
507 analysis was performed as previously described [4].

508

509 **Cell lines, cell isolation, culture and stimulation**

510 The HEK293T cell line was from the American Type Culture Collection (ATCC). Human PBMC samples
511 were generated from peripheral blood samples using gradient centrifuging with LSM™ lymphocyte
512 separation medium (MP Bio, Cat.50494X). Then primary T lymphocytes and monocytes were isolated
513 from PBMCs by negative selection using Pan T Cell Isolation Kit (Miltenyi Biotec, 130-096-535) and

514 Pan Monocyte Isolation Kit (Miltenyi Biotec, 130-096-537) according to manufacturer's instructions.
515 SV40-HDFs were derived from skin biopsies of patient or control donors as described and transformed
516 by lentiviral transduction of SV40-large T antigen.
517 The HEK293T cells, SV40-HDFs were cultured in Dulbecco's Modified Eagle Medium (DMEM, Gibco)
518 supplemented with 10% FBS. Human PBMCs, primary T cells and monocytes were cultured in RPMI
519 1640 (Gibco) supplemented with 10% FBS. HT-29 cells were cultured in McCoy's 5A medium (Gibco)
520 supplemented with 10% FBS.
521 Recombinant human TNF (Peprotech, 300-01A) was used to stimulate HT-29 cells (20 ng ml^{-1}), SV40-
522 HDFs (20 ng ml^{-1}) and human primary monocytes (50 ng ml^{-1}) for the indicated times. z-VAD-fmk
523 (Selleck, S7023, 25 μM), SM-164 (Selleck, S7089, 250 nM) and Nec-1s (Selleck, S8641, 10 μM) were
524 used to treat HT-29 cells, human primary T cells and monocytes. Staurosporine (MCE, HY-15141, 100
525 nM) and RSL3 (Selleck, S8155, 1 μM) were used to induce apoptosis or ferroptosis in T cells.
526
527 **Flow cytometry**
528 Cells were washed with FACS buffer (0.5% BSA in PBS) and blocked with human Fc Block (BD
529 Biosciences, 564219) followed by staining with antibodies against surface molecules in dark for 30 min
530 at 4 °C. Then cells were washed twice and stained with Fixable Viability Stain 780 (BD Biosciences,
531 565388) to distinguish live versus dead cell. For intracellular staining, cells were fixed and permeabilized
532 with BD Phosflow™ Fix Buffer and Perm Buffer (BD Biosciences: 557870, 558052) and then washed
533 twice and stained with antibodies against intracellular antigens for 30 min at 4 °C. For pRIPK1 (Ser166)
534 and cleaved caspase-3 staining, cells were incubated with Alexa Fluor 647 labeled goat anti-rabbit IgG
535 (Thermo, A-21244) for 30 min at 4°C after primary antibody staining. Cells were acquired on CytoFlex
536 (Beckman) and data were analyzed using FlowJo software. The following antibody clones were used for
537 staining in flow cytometry analysis: CD3 (SK7, BD Biosciences), CD4 (RPA-T4, BD Biosciences), CD8
538 (RPA-T8, BD Biosciences), CD14 (M5E2, BD Biosciences), CD16 (3G8, BD Biosciences), CD19
539 (SJ25C1, BD Biosciences), CD56 (NCAM16.2, BD Biosciences), IL-1β (JK1B-1, BioLegend), TNF
540 (MAb11, BD Biosciences), IL-6 (MQ2-13A5, BD Biosciences), IFNγ (4S.B3, BD Biosciences), Cleaved
541 Caspase-3 (Asp175) (CST, #9661), pRIPK1(Ser166) (D8I3A, CST), RIPK1 (D94C12, CST).
542
543 **RNA isolation and real-time RT-PCR**

544 Total RNA from cells was extracted using a RNeasy Mini Kit (Qiagen, 74104) according to the
545 manufacturer's instructions. 1 μg RNA was reverse transcribed into cDNA with ReverTra Ace® qPCR
546 RT Master Mix (TOYOBO, FSQ-301). cDNA was then diluted and used for real-time PCR using 2x
547 Universal SYBR Green Fast qPCR Mix (Abclonal, RK21203) with primers targeting *IL1B* (F, 5'-
548 TGCTCTGGGATTCTCTTCAGC-3'; R, 5'-AAGTCATCCTCATTGCCACTGT-3'), *IL6* (F, 5'-
549 CATCCTCGACGGCATCTCAG-3'; R, 5'-ACCAGGCAAGTCTCCTCATTG-3'), *IL8* (F 5'-
550 CCAAACCTTTCCACCCCAAA-3'; R, 5'-GAATTCTCAGCCCTCTTCAAAAAC-3') *TNF* (F, 5'-
551 CTCTTCTGCCTGCTGCACTTTG-3'; R, 5'-ATGGGCTACAGGCTTGTCACTC-3'), and *GAPDH* (F,
552 5'-TCGACAGTCAGCCGCATCTTC-3'; R, 5'-GCGCCCAATACGACCAAATCC-3'). Relative
553 transcription levels were calculated by normalization to *GAPDH* mRNA.
554
555 **Cell viability assay and cell death assay**
556 Primary T cells (15000 cells/well), SV40-HDFs (2000 cells/well) or HT-29 (5000 cells/well) were plated
557 in 384-well plate and were stimulated with indicated conditions. General cell viability was measured by
558 using CellTiter-Glo® Luminescent Cell Viability Assay (Promega, G7572) according to the
559 manufacturer's instructions. The percentage of viability was normalized to untreated controls. Cell death
560 detection was performed by direct staining with 0.5 μg/ml Propidium Iodide (PI) and 0.5 μg/ml DAPI
561 for 10 min and imaging with fluorescence microscope. PI positive dead cell was counted and normalized
562 to DAPI counts. For continuous cell death measurement, cells were simulated with indicated conditions
563 and stained with 200 nM Hoechst 33342 (Beyotime, C1022) and 200 nM SYTOX™ Orange (Thermo,
564 S34861) at the same time. The percentage of dead cell was assayed every 1 hour by imaging with BioTek
565 Cytation 3 for 18 hours with 5% CO_2 and 37 °C condition. Results were exported as counts per well to
566 be processed and graphed using Prism 9.
567
568 **Protein array**
569 Semiquantitative analysis of 174 cytokine levels of P2's serum samples before (normal stage) or after
570 (onset, non-flare) the first onset of fever was performed with human Cytokine Array G2000 (RayBiotech)
571 by Novogene Company (Beijing, China). Generally, the cytokine array glass slides were firstly blocked
572 for 1 hour at room temperature and then incubated with 100 μl serum samples at 4 °C overnight. On the
573 second day, the slides were washed with wash buffer and incubated with Biotin-Conjugated Anti-

574 Cytokines and HiLyte Plus™ 555 Streptavidin-Fluor according to the manufacturer's instructions. The
575 results were scanned with InnoScan 300 Microarray Scanner (Innopsys) at 532 nm with 10 μm resolution.
576 The mean fluorescence intensity (MFI) was calculated and exported for further analysis.
577
578 **Human and mouse cytokines measurement**
579 Human or mouse serum cytokines were measured by enzyme-linked immunosorbent assay (ELISA)
580 (Multi Sciences: 70-EK1280, 70-EK194, 70-EK182HS, 70-EK106HS, 70-EK191, 70-EK180HS, 70-
581 EK1F01, 70-EK1F02, EK206HS, EK282HS/2) according to the manufacturer's instructions. T cell
582 culture supernatant cytokines were determined by Cytometric Bead Arrays (BD Biosciences) according
583 to the manufacturer's instructions. Human serum adenosine deaminase (ADA) activity was measured
584 with Boyle colorimetric method by using ADA Activity Assay Kit (Yuanye Bio, R22207) according to
585 the manufacturer's instructions. Student's t-test was performed for the statistical analysis.
586
587 ***In vitro* cell proliferation assay**
588 Fresh isolated $CD3^+$ T cells were labeled with CFSE (Thermo, 65-0850-84, 5 μM) and then stimulated
589 with anti-CD3/CD28 beads (T&L Biotechnology) at 1:1 ratio supplemented with hrIL-7 (PrimeGene)
590 and hrIL-15 (PrimeGene) in 48-well plates for 96 hours. Then all cells were co-stained with CD4-BB515
591 and CD8-BV510 antibodies and analyzed using CytoFlex (Beckman).
592
593 **Gene editing of patient T cells**
594 Primary T cells isolated from patients were stimulated with anti-CD3/CD28 beads for 3 days. For
595 electroporation, 180 pmol sgRNA and 25 μg Cas9 protein were mixed and incubated for 15 min at room
596 temperature for ribonucleoprotein complexes (RNP) formation. Then 3e6 T cells resuspended in opti-
597 MEM were mixed with RNP and 6 μg dsDNA template and electroporated using Gemini X2 (BTX)
598 under the #905 program for human primary T cells. After electroporation, 1 ml warm X-VIVOTM 15
599 Serum-free Hematopoietic Cell Medium (Lonza) supplemented with 10% FBS was immediately added
600 to the cuvette and the mixture was then carefully transferred to 24-well plates for further culture and
601 analysis.
602
603 **T cell-MDM co-culture assay**

604 Freshly isolated monocytes were seeded in 24-well plate and differentiated into monocyte-derived
605 macrophages (MDMs) with 20 ng/ml GM-CSF treatment for 10 days. Then, 0.4 μm pore polycarbonate
606 membrane inserts containing T cells isolated from PBMCs of patient or healthy donors were placed into
607 the 24-well plate for the T cell-MDM co-culture at the ratio of 5:1 for 8 hours. Finally, T cells were
608 removed and bottom MDMs were collected for mRNA extraction.
609
610 **Mice**
611 All mouse studies complied with relevant ethical regulations and approved by Institutional Animal Care
612 and Use Committee (IACUC) of the Zhejiang University (Registration No.:27043). The *Cd8a*-creERT2
613 and *Lyz2*-creERT2 strains on C57BL/6J background were purchased from GemPharmatech. The *Rosa26*-
614 mTmG strain on C57BL/6J background was purchased from Cyagen. All mice were maintained under
615 specific pathogen-free condition with free access to food and water at Laboratory Animal Center of
616 Zhejiang University.
617
618 **HSC isolation, transduction, transplantation, induction and LPS challenge**
619 Mouse hematopoietic stem cells (HSC) were isolated from 6- to 8-week-old donor mice using Lineage
620 cell depletion kit (Miltenyi Biotec, 130-090-858) according to manufacturer's instruction. HSCs were
621 plated in 12-well plate and were transduced with lentivirus carrying human RIPK1 inducible expression
622 system (MOI=50). Transduction efficiencies were measured with flow cytometry after 24 hours culturing
623 and 200,000 of transduced HSCs were transplanted into lethally irradiated (4 Gy, 2 times) recipient mice
624 (female, 8 to 12 weeks old). Transplantation efficiencies were validated by flow cytometry analysis after
625 2 weeks. Successfully transplanted mice were injected i.p with 20 mg/ml tamoxifen (MCE, HY-13757A)
626 dissolved in corn oil (MCE, HY-Y1888) every two days for 5 times to induce the expression of WT,
627 K377E, R390G or D324V mutated RIPK1. Then, these mice were injected i.p with 0.5 mg/kg
628 lipopolysaccharide (LPS) (Sigma, L6529) and serum were collected before injection or injected for 2
629 hours. Serum Il6 and Tnf were measured by ELISA as described.
630
631 **Immunoprecipitation and western blot**
632 For TNFR signaling complex (TNF-RSC) enrichment, 5e6 cells were seeded and treated with flag tagged
633 TNF (ENZO, ALX-522-008) for indicated times. The samples were immediately washed with cold PBS

634 and lysed in cold lysis buffer (25 mM Tris-HCl, pH 7.4, 150 mM NaCl, 0.5% NP-40, 10% glycerol) with
635 freshly added inhibitors blocking protease and phosphatase (Merck: 4906837001, 4693159001) for 30
636 min. Then samples were cleared through centrifugation at 20000 RCF for 10 min and protein
637 concentrations were determined by Pierce™ BCA Protein Assay Kits (Thermo, 23225). Then the TNF-
638 RSC was immunoprecipitated with FLAG M2 magnetic beads (Sigma, M8823) at 4 °C for 4 hours and
639 the protein complex was directly eluted by boiling in 1×SDS loading buffer. For TNF downstream
640 signaling analysis, 4e5 cells were seeded and treated as indicated and then cells were harvested and lysed
641 directly with sample loading buffer. These samples were separated through routine SDS-PAGE and
642 transferred to 0.45 μm nitrocellulose membrane (Cytiva, 10600002) and blotted with indicated antibodies.
643
644 **CyTOF**
645 PBMCs were freshly isolated from whole bloods of four patients (P1 and P2; CRIA-1 and CRIA-2) and
646 four unaffected controls, then blocked and labeled with conjugated antibodies as described[31]. Fixed cell
647 samples were resuspend analyzed on a mass cytometer (Helios, Fluidigm). The CyTOF data exported
648 as FCS files were gated in FlowJo (v10.0.7) to remove doublets and $CD45^+$ single cells identified by
649 DNA (^{191}Ir and ^{193}Ir)、^{194}Pt and event length. For downstream analysis, 10,000 cells were randomly
650 selected from each sample. The raw values of FCS files were transformed using the arcsinh function
651 with a cofactor of 5. Phenograph clustering in cytofkit R package was performed on all subsampled
652 sample events and the transformed values of all events were subjected to t-SNE dimension reduction
653 using R-tsne package[32,33].
654
655 **Antibodies**
656 The following antibodies were purchased from Cell Signaling Technology: pRIPK1 (S166) (65746),
657 RIPK1 (3493), pMLKL (S358) (91689), MLKL (14993), pIKKα/β (S176/180) (2697), IKKβ (2370),
658 Sharpin (12541), pp65 (S65) (3033), p65 (8242), pIκBα (S32) (2859), IκBα (4814), pERK1/2
659 (T202/Y204) (4370), ERK1/2 (4695), pJNK (T183/Y185) (9251), JNK (9252), HA (3724), cleaved
660 caspase-3 (D175) (9661), caspase-3 (9662). NEMO (sc-8330) was purchased from Santa Cruz
661 Biotechnology. GAPDH (SA30-01) was purchased from HUABIO.
662
663 **Data availability**

664 The raw data of sequencing will be available prior to publication. The other source data that support the
665 findings of this study are available from the corresponding author upon reasonable request.
666

667 30 Carmona-Rivera, C. & Kaplan, M. J. Induction and Quantification of NETosis. *Curr Protoc*
668 *Immunol* **115**, 14 41 11-14 41 14 (2016). https://doi.org:10.1002/cpim.16
669 31 Wang, Y. *et al.* Identification of an IL-1 receptor mutation driving autoinflammation directs IL-
670 1-targeted drug design. *Immunity* **56**, 1485-1501 e1487 (2023).
671 https://doi.org:10.1016/j.immuni.2023.05.014
672 32 Levine, J. H. *et al.* Data-Driven Phenotypic Dissection of AML Reveals Progenitor-like Cells
673 that Correlate with Prognosis. *Cell* **162**, 184-197 (2015).
674 https://doi.org:10.1016/j.cell.2015.05.047
675 33 Chen, H. *et al.* Cytofkit: A Bioconductor Package for an Integrated Mass Cytometry Data
676 Analysis Pipeline. *PLoS Comput Biol* **12**, e1005112 (2016).
677 https://doi.org:10.1371/journal.pcbi.1005112

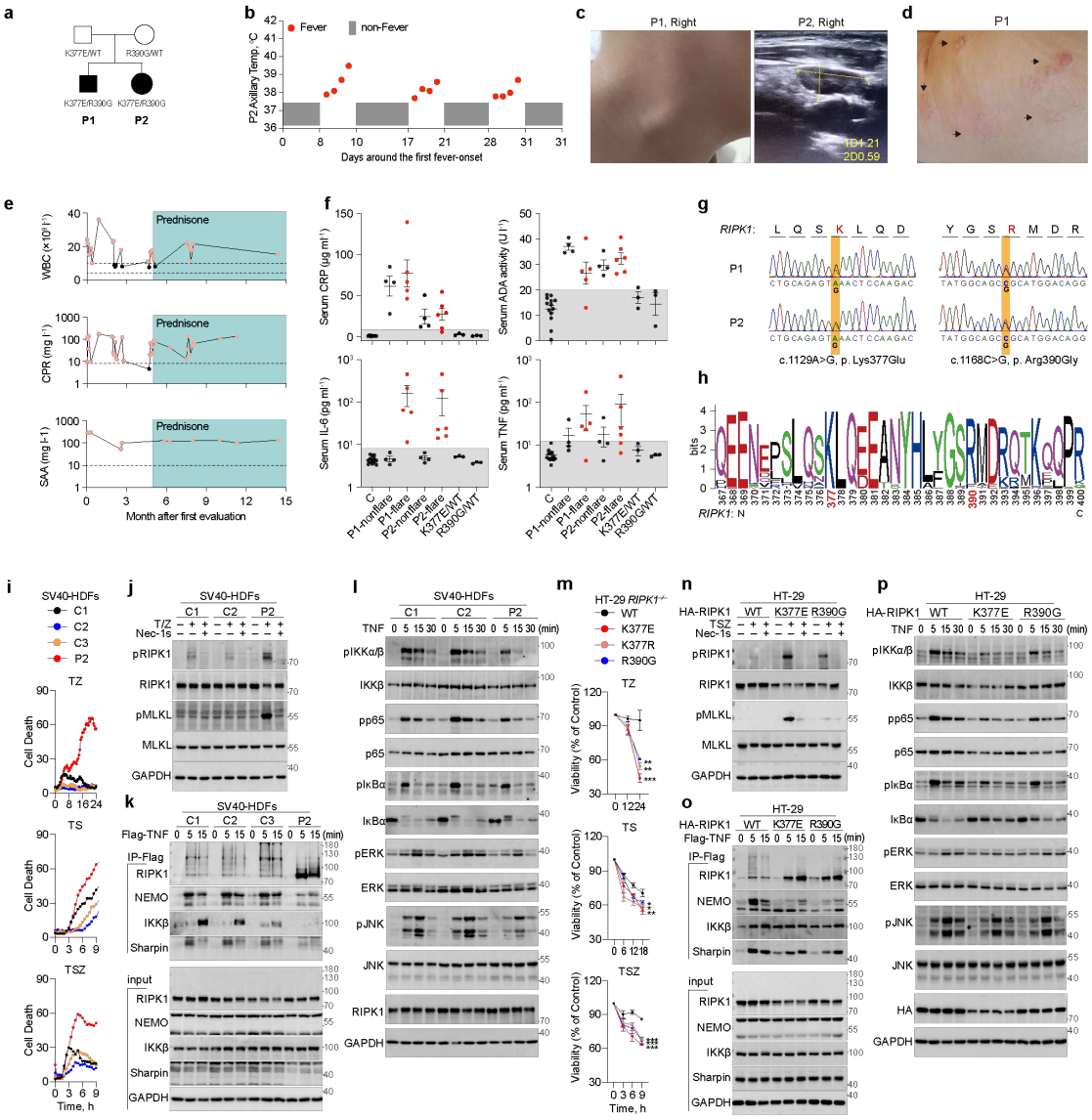

Fig. 1 | Compound heterozygous gain-of-function mutations in *RIPK1* causes systemic autoinflammatory diseases.

a, Pedigrees of a family with two patients carrying mutations at *RIPK1* K377 and R390. Patient 1 (P1) and patient 2 (P2) were represented with filled symbols. **b,** Timeline of recurrent fever episodes in P2 over 5 weeks. Red dots represented increased temperatures during fever episodes and grey boxes represent the normal temperatures between flares. **c,** Representative sonographic image showing lymphadenopathy of P2. The diameters of right cervical lymph nodes were marked with dotted yellow line. **d,** Representative macroscopic image of dermatological manifestations in P1 during acute phase reaction, showing skin rashes (arrows). **e,** Whole blood cell counts (WBC), C-reactive protein (CRP) and serum amyloid A protein (SAA) were measured serially after the first evaluation of P1 and prednisone treatment (cyan shading) started at the age between 0-5. Horizontal dotted lines indicate age-specific

690 high values for CRP, SAA or high and low values for WBC count. Red dots donate the abnormal values.
691 **f,** C-reactive protein (CRP), serum ADA enzymatic activity and IL-6, TNF levels of unaffected controls
692 (C, n=13), P1 during prednisone treatment (4 samples taken during flare and 5 samples taken during non-
693 flare), P2 (4 samples taken during flare and 6 samples taken during non-flare), unaffected parents
694 carrying heterozygous K377E mutation (K377E/WT, 1 sample from I-2 and 2 samples from II-2) or
695 R390G mutation (R390G/WT, 3 samples from II-3). **g,** Sanger sequencing chromatograms of *RIPK1*
696 showed heterozygous base substitutions at p. K377E and p. R390G in whole blood genomic DNA from
697 P1 and P2. **h,** WebLogo demonstrating conservation of human *RIPK1* K377 and R390 across 42
698 vertebrate species. **i-l,** Cell death of SV40-immortalized human dermal fibroblasts (SV40-HDFs) isolated
699 from three unaffected controls (C1-C3) and P2 were monitored by continuous imaging of SYTOX™
700 Orange staining. The SV40-HDFs were treated with T, S, Z as indicated (**i**). SV40-HDFs was treated
701 with TZ with or without Nec-1s (10 μM) for 12 hours and immunoblotted with indicated antibodies (**j**).
702 The TNFR signaling complex (TNF-RSC) were immunoprecipitated with Flag-TNF for 5 or 15 min and
703 immunoblotted with indicated antibodies (**k**). NF-κB and MAPK activation of SV40-HDFs treated with
704 TNF for 5, 15 or 30 min immunoblotted with indicated antibodies (**l**). **m-p,** *RIPK1*$^{-/-}$ HT-29 cells were
705 lentivirally complemented with HA-RIPK1 wild-type (WT), K377E, R390G and treated with T, S, Z as
706 indicated. Cell viability was measured by CellTiter-Glo luminescent cell viability assay (**m**)**.** The
707 necroptosis markers (**n**), TNF-RSC (**o**) and the NF-κB and MAPK activation (**p**) were analyzed in the
708 same way. T denotes 20 ng ml^{-1} TNF; S denotes 250 nM SM-164; Z denotes 25 μM z-VAD-fmk. Graphs
709 show mean±SD. Statistical significance was determined by one-way ANOVA (**m**), **P < 0.01, ***P <
710 0.001.
711

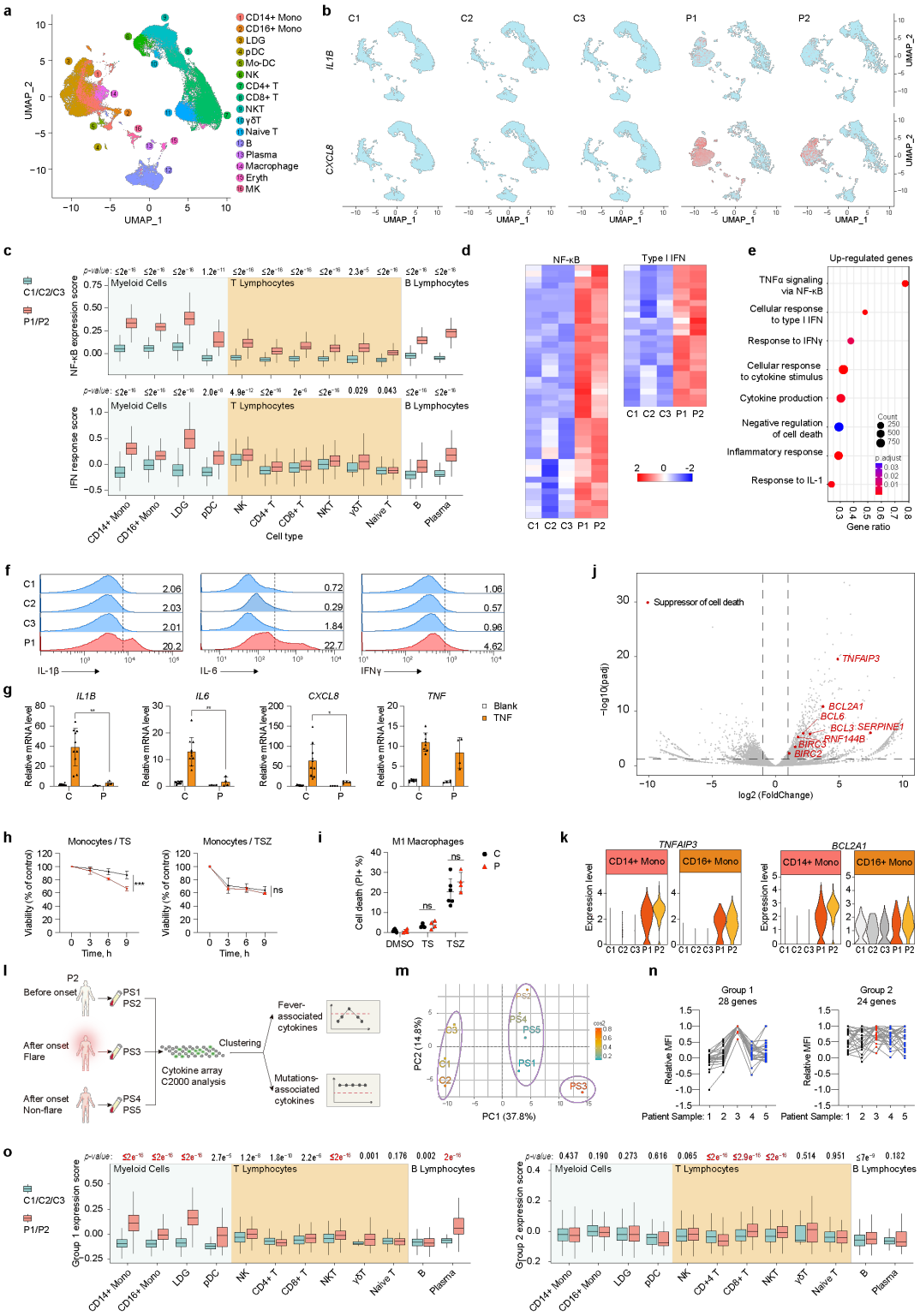

Fig. 2 | Strong activation of inflammatory signaling in myeloid cells carrying *RIPK1* mutations.

a, Integrated uniform manifold approximation and projection (UMAP) visualization of peripheral blood mononuclear cells (PBMCs) from three unaffected controls (C1, n=13925 cells; C2, n=11117 cells; C3, n=12573 cells) and two patients (P1, n=10918 cells; P2, n=8516 cells), marker-based annotation of 15 cell subtypes were colored by cluster identity. LDG, low-density granulocyte; pDC, plasmacytoid

718 dendritic cell; Mo-DC, monocyte-derived dendritic cell; NK, natural killer cell; NKT, natural killer T
719 cell; Eryth, erythrocyte; MK, megakaryocyte. **b,** Visualization of expressions of *IL1B* and *CXCL8*
720 (colored single cells) projecting PBMCs from unaffected controls (C1-C3) and two patients (P1 and P2)
721 on UMAP plots. **c,** Boxplots of the NF-κB expression score (top panel) and IFN response score (bottom
722 panel) of cell subtypes. **d,** Heatmap of representative genes downstream of NF-κB and type I IFN
723 pathways in monocyte compartments. Gene names were listed in Extended Data Fig.4d. **e,** Dot plot
724 showing the biological processes identified with un-regulated gene terms (FDR <0.05) in patients'
725 monocytes compared to that of unaffected controls using DAVID. The size of the circle indicates the
726 gene count enriched in the pathway and the color represents pathway enrichment significance. **f,**
727 Intracellular cytokine analysis of IL-1β, IL-6 and IFNγ in monocytes isolated from three unaffected (C1-
728 C3) controls and P1. **g,** qRT-PCR analysis of *IL1B, IL6, CXCL8* and *TNF* mRNA levels in primary
729 monocytes isolated from unaffected controls (n=8-10) and two patients (n=4 from P1 and P2) with or
730 without 10 ng ml^{-1} TNF for 6 hours. **h,** CellTiter-Glo luminescent cell viability detection of primary
731 monocytes isolated from unaffected controls (n=12) and two patients (n=3 from P1 and P2) stimulated
732 with T, S, Z for indicated times. **i,** Statistics of dead M1 macrophages stimulated with TS or TSZ for 24
733 hours by imaging of propidium iodide (PI). M1 macrophages were differentiated from primary
734 monocytes of unaffected controls (n=6) and two patients (n=4 from P1 and P2). Representative images
735 were presented in Extended Data Fig.3e. **j,** Volcano plot displaying the differentially expressed genes in
736 monocyte compartments between three unaffected controls (C1-C3) and two patients (P1 and P2).
737 Representative suppressive genes of cell death were labeled with red dots and gene names. **k,** Clusters in
738 the monocyte compartments showing the expression levels of *TNFAIP3* and *BCL2A1* in three unaffected
739 controls (C1-C3) and two patients (P1 and P2). **l,** Schematic diagram showing serum cytokine microarray
740 analysis of continuous P2's serum samples before (PS1 and PS2) or after (PS3, flare; PS4 and PS5, non-
741 flare) the onset of recurrent fever. **m,** PCA analysis of sample variance determined by semi-quantitative
742 174 cytokines antibody array on serum samples of C1-C3 from three unaffected controls and PS1-PS5
743 from P2. **n,** The integrated relative MFI plots of P2's serum cytokine levels. 28 cytokines peaked in PS3
744 were enrich in group 1, 24 cytokines higher than control were enriched in group 2. **o,** Boxplots exhibiting
745 mRNA expression scores of cytokines of group 1 (left panel) and group 2 (right panel) in indicated cell
746 compartments. Group 1 and group 2 cytokine panels were clustered with the serum cytokine microarray
747 analysis in Extended Data Fig.4. T denotes 10 ng ml^{-1} TNF; S denotes 250 nM SM164; Z denotes 25 μM

748 z-VAD-fmk. All histogram graphs show mean±SD. Statistical significance was determined by two-tailed

749 unpaired t-test (**c, g, i, l**) or one-way ANOVA (**h**), ns, $P > 0.05$, *$P<0.05$, **$P < 0.01$, ***$P < 0.001$.

750

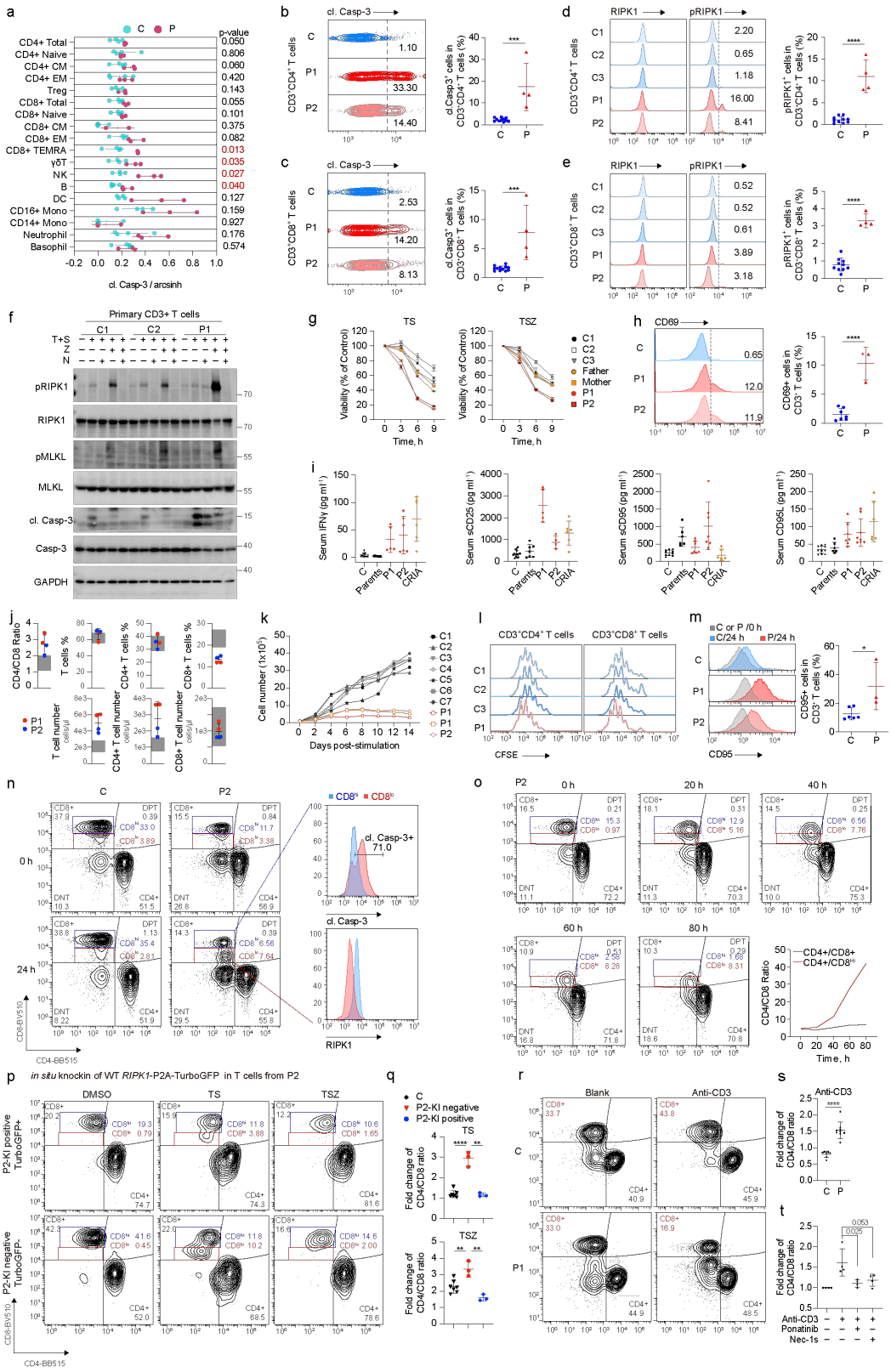

Fig. 3 | Increased cell death and CD4/CD8 ratio in T cells caused by RIPK1 activation.

a, Average expression values (arcsinh transformed) of cl. Casp-3 across identified peripheral immune cell lineages in PBMCs freshly isolated from four unaffected controls (C) and two patients (P, 1 sample from P1 and 2 samples from P2) by mass cytometry by time-of-flight (CyTOF) analysis. **b-e,**

756 Representative contour plots of cl. Casp-3 (**b-c**) and histograms of total RIPK1, pRIPK1(S166) (**d-e**)
757 levels in $CD4^+$ T and $CD8^+$ T cells in freshly isolated PBMCs from unaffected controls (n=10-12) and
758 patients (n=4 for P1 and P2) (left panel). Summary histograms of cl. Casp-3 and pRIPK1(S166) (right
759 panel) were shown. **f,** Immunoblotting analysis of primary $CD3^+$ T cells isolated from two unaffected
760 controls (C1 and C2) and P1 treated with T and S with or without Z, N for 6 hours. Antibodies as indicated
761 were immunoblotted to show the activation of apoptosis or necroptosis. **g,** CellTiter-Glo luminescent cell
762 viability detection of primary $CD3^+$ T cells isolated from three unaffected controls (C1-C3), two patients
763 (P1 and P2) and their parents treated with TS or TSZ for indicated times, n=4. **h,** Representative
764 histogram and statistical analysis of surface CD69 expression on $CD3^+$ T cells from unaffected controls
765 (n=7) and two patients (n=3 for P1 and P2). **i,** Serum IFNγ, sCD25, sCD95 and CD95L of unaffected
766 controls (C, n=10), two patients (P1, n=5-7; P2, n=4-8) and their parents (n=6-7) as well as two CRIA
767 syndrome patients (n=6) determined by ELISA. **j,** CD4/CD8 ratio in T cells, percentages and absolute
768 counts of $CD3^+$ T, $CD4^+$ T, $CD8^+$ T cells in whole blood sample of P1 (red dots) and P2 (blue dots)
769 measured using immunophenotyping. **k,** *In vitro* expansion of primary T cells isolated from unaffected
770 controls (n=7) and patients (n=3 for P1 and P2) as indicated. Cell numbers were counted every two days
771 post anti-CD3/CD28 dynabeads stimulation. **l,** Proliferation of $CD4^+$ T and $CD8^+$ T cells isolated from
772 three unaffected controls (C1-C3) and P1 were analyzed using CFSE staining upon stimulation with anti-
773 CD3/CD28 dynabeads for 96 hours. **m,** Representative histograms of surface CD95 expression on $CD3^+$
774 T cells analyzed with flow cytometry after culturing *in vitro* for 24 hours. **n,** Representative contour plots
775 depicting the percentages of $CD4^+$ T, $CD8^+$ T, double negative T (DNT) and double positive T (DPT) in
776 $CD3^+$ T cells gated from PBMCs of P2 culturing *in vitro* for 24 hours. Histograms displaying cl. Casp-3
777 and RIPK1 expression levels in $CD8^{hi}$ T and $CD8^{lo}$ T cells. **o,** Representative contour plots and summary
778 histograms showing percentages of $CD4^+$ T, $CD8^+$ T and $CD8^{hi}$ T cells and CD4/CD8 ratio in $CD3^+$ T
779 cells isolated from P2 cultured for indicated times. **p-q,** Representative contour plots showing
780 percentages of $CD4^+$ T, $CD8^+$ T in $CD3^+$ T cells of P2 with ($TurboGFP^+$) or without ($TurboGFP^-$)
781 restoration using CRISPR/Cas9-mediated *in situ* knock-in of WT *RIPK1-P2A-TurboGFP* under
782 stimulation of T with or without S, Z for 6 hours (**p**). CD4/CD8 ratio in $CD3^+$ T cells of unaffected
783 controls (n=7) and two patients (n=3 for P1 and P2) were quantified (**q**). **r-s,** Representative contour plots
784 (**r**) and statistical analysis (**s**) showing percentages of $CD4^+$ T, $CD8^+$ T, DNT and DPT cell in $CD3^+$ T
785 cells isolated from unaffected control (n=7) and two patients (n=9 for P1 and P2) under the stimulation

786 of anti-CD3 antibody (5 μg ml^{-1}) for 72 hours. **t,** Statistical analysis of fold change of CD4 /CD8 ratio in
787 $CD3^+$ T cells isolated from two patients (n=4 for P1 and P2) under stimulation of anti-CD3 antibody (5
788 μg ml^{-1}) with or without 250 nM Ponatinib or 10 μM Nec-1s for 24 hours. For representative contour
789 plots, see Extended Data Fig. 6h. T denotes 10 ng ml^{-1} TNF; S denotes 250 nM SM164; Z denotes 25
790 μM z-VAD-fmk; N denotes 10 μM Nec-1s. All histogram graphs show mean±SD. Statistical significance
791 was determined by one-way ANOVA (**g**) or two-tailed unpaired t-test in the rest, *P<0.05, **P < 0.01,
792 ***P < 0.001, ****P < 0.0001.
793

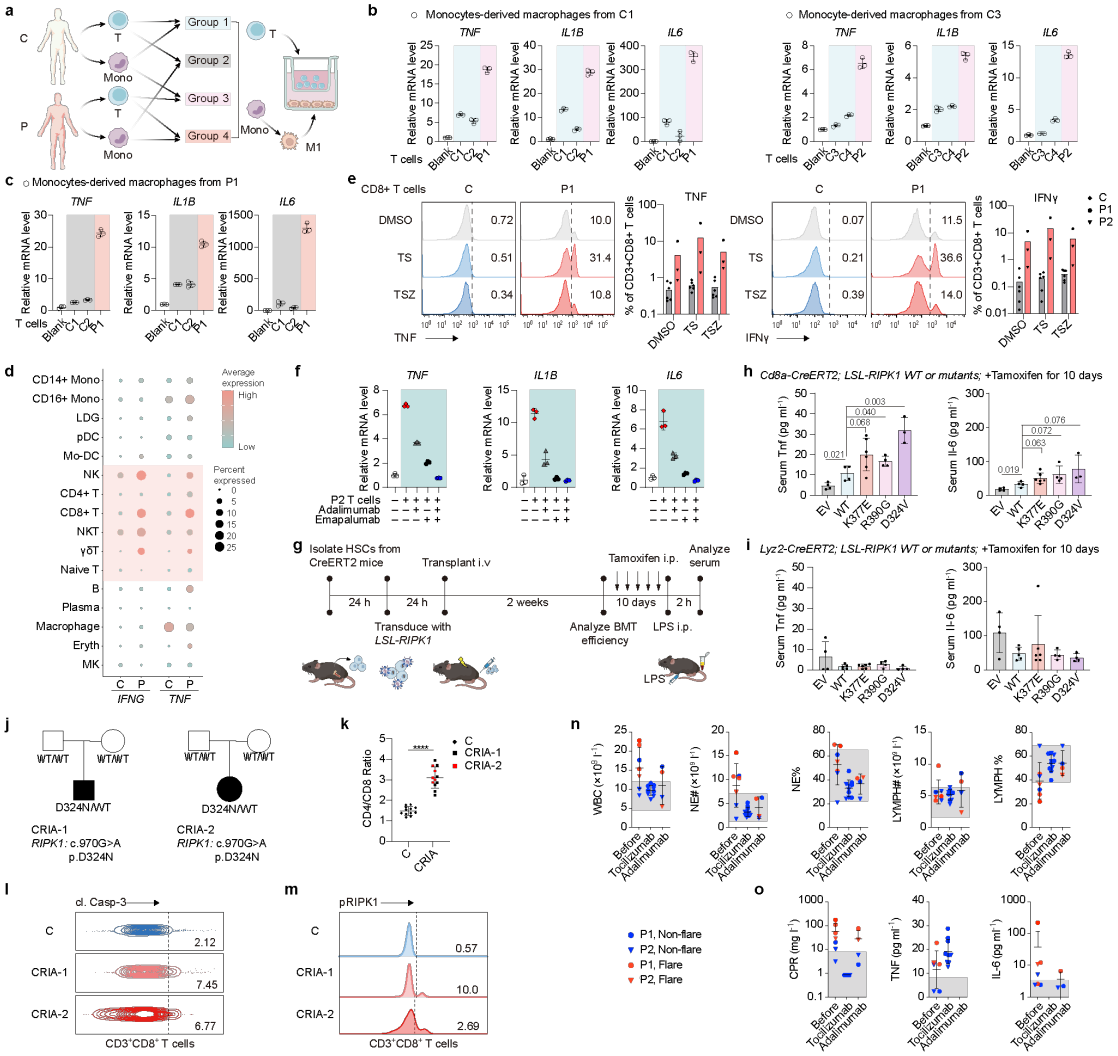

Fig. 4 | RIPK1 activation causes inflammation through T-Mono axis.

a, Schematic diagram of T cell-MDM co-culture system. **b-c,** qRT-PCR analysis of *TNF, IL1B* and *IL6* mRNA levels in GM-CSF-activated monocytes derived macrophages (MDMs) co-cultured with or without T cells for 6 hours. GM-CSF-activated MDMs generated from unaffected control 1 (C1) (left panel) or unaffected control 3 (C3) (right panel) (**b**) or P1 (**c**) were co-cultured with donor-matched T cells as well as T cells from other unaffected controls (C2 and C4) or patients as indicated. **d,** Dot plot of *IFNG, TNF* in cell subtypes found in scRNA-seq of PBMCs from three unaffected controls and two patients. The size of the circle indicates the percentage of cells positive for gene expression and the color represents the average expression level. **e,** Representative histograms and statistical analysis of TNF and IFNγ expression in CD8$^+$ T cells in PBMCs isolated from unaffected controls (n=6) and patients (n=3 for P1 and P2) treated with 10 ng ml^{-1} TNF (T) with or without 250 nM SM-164 (S), 25 μM z-VAD-fmk (Z) for 24 hours. **f,** T cells isolated from P2 were co-cultured with MDMs generated from unaffected

807 control in the presence of 10 μg ml^{-1} adalimumab, 10 μg ml^{-1} emapalumab alone or in combination for 6
808 hours. *TNF, IL1B* and *IL6* mRNA levels of MDMs were analyzed by qRT-PCR. **g,** Experimental timeline
809 for generation of HSCs-transplanted mice with conditional overexpression of human WT or mutated
810 RIPK1 K377E, R390G or D324V in $CD8\alpha^+$ T cell- or myeloid cell-specific lineage. **h-i,** ELISA
811 measurement of serum Tnf and Il6 levels in mice specifically overexpressing WT or mutated hRIPK1 in
812 $CD8\alpha^+$ T cells (**h**) or myeloid cells (**i**). **j-m,** Pedigrees of two families with CRIA patients (CRIA-1 and
813 CRIA-2) (**j**). Patients were represented with filled symbols. Summary histograms of CD4/CD8 ratio in
814 $CD3^+$ T cells of unaffected controls (n=12), CRIA-1 (n=7) and CRIA-2 (n=5) were shown (**k).**
815 Representative contour plots of cl. Casp-3 (**l**) and histograms of pRIPK1(S166) (**m**) protein levels in
816 $CD8^+$ T cells in freshly isolated PBMCs from CRIA patients. **n-o,** Whole blood cell counts (WBC), cell
817 counts and proportions of neutrophil (NE#-NE%) and lymphocyte (LYMPH# -LYMPH%) (**n**), Serum
818 C-reactive protein (CRP), TNF and IL-6 (**o**) of P1 (red dots) and P2 (blue dots) measured before and
819 after tocilizumab or adalimumab treatments. The grey area represents the range of unaffected controls.
820 Dots represent each sample and graphs show mean±SD. Statistical significance was determined by two-
821 tailed unpaired t-test, $*P<0.05$, $**P < 0.01$, $***P < 0.001$, $****P < 0.0001$.
822

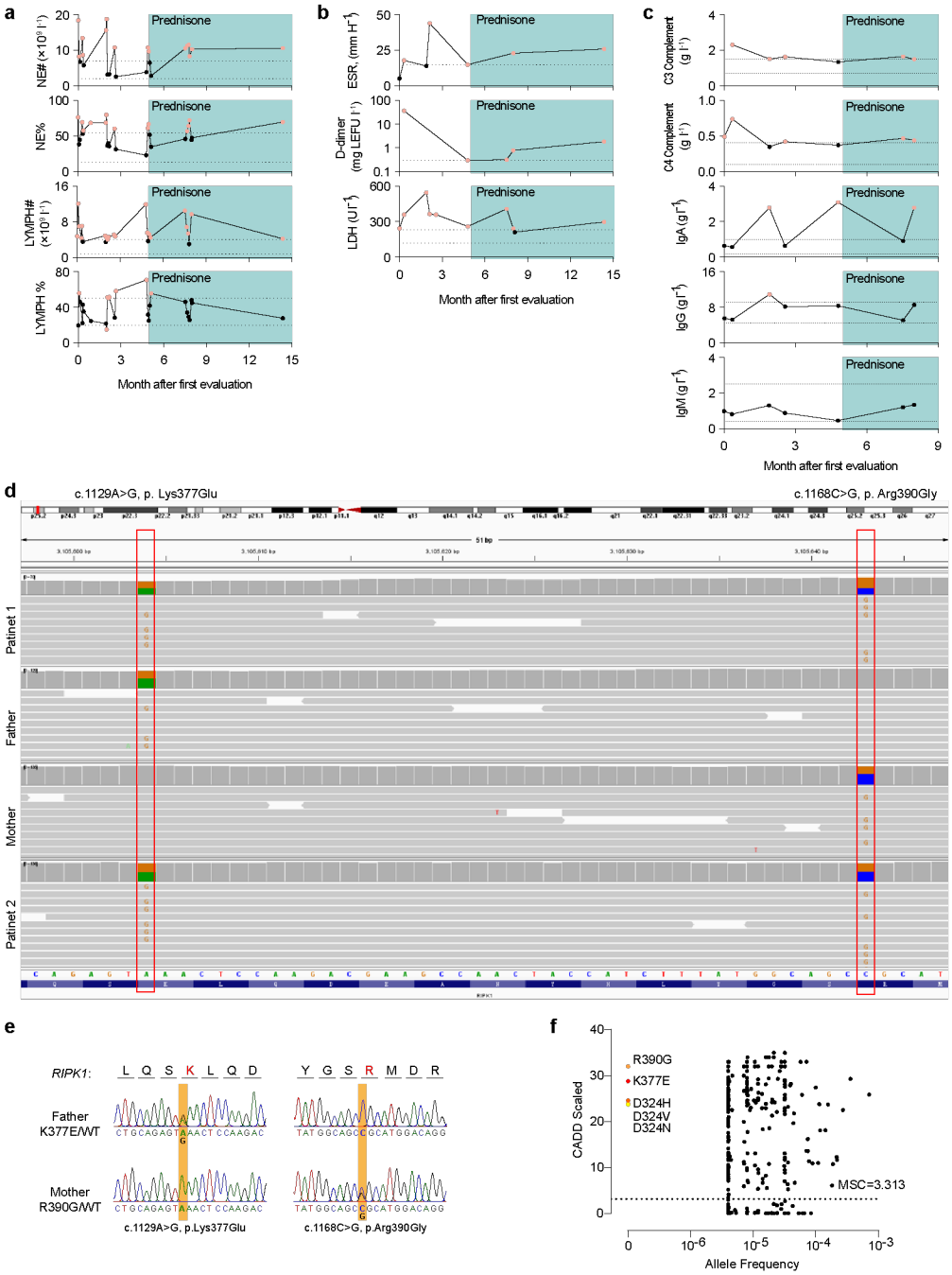

Extended Data Fig. 1 | Clinical and genetic information of autoinflammatory patients carrying compound heterozygous GOF mutations in *RIPK1*.

a-c, Cell counts and proportions of neutrophil (NE#-NE%) and lymphocyte (LYMPH# -LYMPH%) (**a**), erythrocyte sedimentation rate (ESR), D-dimer, serum lactate dehydrogenases (LDH) (**b**), serum C3 complement, C4 complement, IgA, IgG, IgM (**c**) measured serially after the first evaluation of P1 and prednisone treatment (cyan shading) started at the age between 0-5. Horizontal dotted lines indicating age-specific high values for ESR, D-dimer or high and low values for the rest tests. Red dots donate the abnormal values. **d,** Whole exome sequencing reads covering *RIPK1* p. Lys377Glu (NM_003804.4:

832 c.1129A>G) and p. Arg390Gly (NM_003804.4: c.1168C>G) variants in two patients and their parents
833 displayed using integrative genomics viewer. **e,** Sanger sequencing chromatograms of *RIPK1* in whole
834 genomic DNA from parents. **f,** Correlating Combined Annotation Dependent Depletion (CADD) scores
835 with minor allele frequencies (MAF) for *RIPK1* K377E, R390G and D324 variants. Mutation
836 significance cutoff (MSC) was show.
837

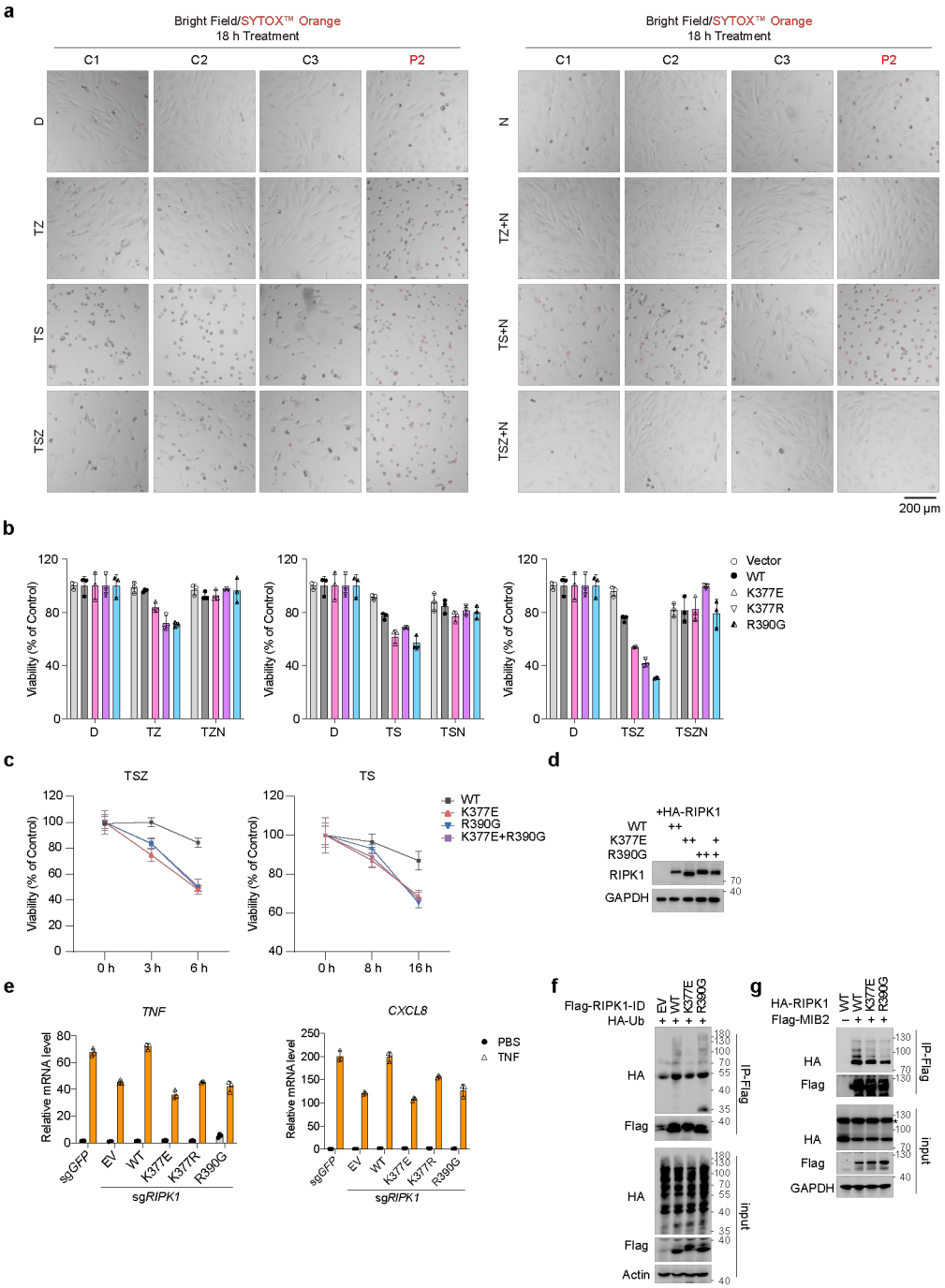

Extended Data Fig. 2 | *RIPK1* mutations sensitize cells to TNF-induced cell death.

a, SV40-HDFs isolated from three unaffected controls (C1-C3) and P2 were treated with T with or without S, Z and N as indicated. Cell death were monitored by imaging of SYTOX™ Orange staining. **b-d,** CellTiter-Glo luminescent cell viability detection of *RIPK1*$^{-/-}$ HT-29 cells complemented with WT or mutated *RIPK1* K377R, K377E, R390G, K377E/R390G under stimulation of TZ, TS, TSZ with or without N as indicated **(b-c)**. Expression levels of WT or mutated RIPK1 were determined with immunoblot **(d)**. **e,** mRNA levels of *TNF*, *CXCL8* in complemented HT-29 cells treated with TNF for 6

846 hours were determined with qRT-PCR. **f-g,** HEK293T cells were transfected with plasmids encoding full
847 length/intermediate domain of RIPK1 together with MIB2 or Ub as indicated. ID domain of RIPK1 or
848 MIB2 were immunoprecipitated with anti-Flag dynabeads and immunoblotted with indicated antibodies.
849 T denotes 20 ng ml^{-1} TNF; S denotes 250 nM SM-164; Z denotes 25 μM z-VAD-fmk; N denotes 10 μM
850 Nec-1s. Graphs show mean±SD.
851

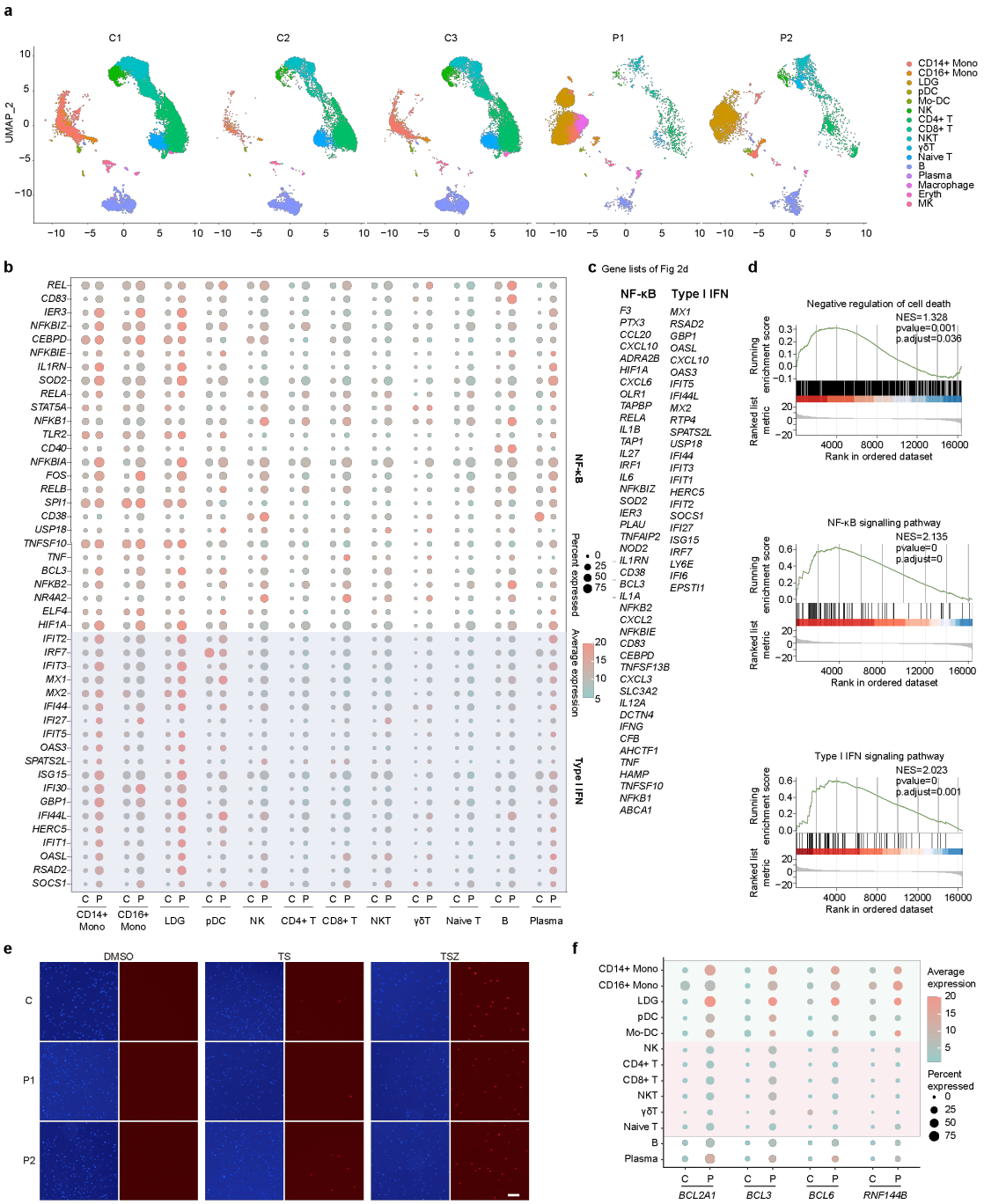

852

853 **Extended Data Fig. 3** | Inflammatory signature in patients' monocytes.

854 **a,** Uniform manifold approximation and projection (UMAP) visualization of peripheral blood
855 mononuclear cells (PBMCs) from three unaffected controls (C1, n=13925 cells; C2, n=11117 cells; C3,
856 n=12573 cells) and two patients (P1, n=10918 cells; P2, n=8516 cells). **b,** Dot plot showing the
857 expression of representative genes downstream of NF-κB and type I IFN pathways in cell subtypes of
858 PBMCs. The size of the circle indicates the percentage of cells positive for target gene expression and
859 the color represents the average expression levels of genes in clusters. **c,** List of gene names in keeping
860 with Fig.2d. **d,** Gene set enrichment analysis (GSEA) plot of negative regulation of cell death

861 (NES=1.328, P<0.01), NF-κB signaling pathway (NES=2.135, P<0.01) and Type I IFN signaling
862 pathway (NES=2.023, P<0.01). NES, normalized enrichment score. **e,** Representative images of dead
863 M1 macrophages in keeping with Fig.2i. **f,** Dot plot of negative regulators of cell death *BCL2A1, BCL3,*
864 *BCL6, RNF144B* in cell subtypes found in scRNA-seq of PBMCs from three unaffected controls and two
865 patients. The size of the circle indicates the percentage of cells positive for gene expression and the color
866 represents the average expression levels.
867

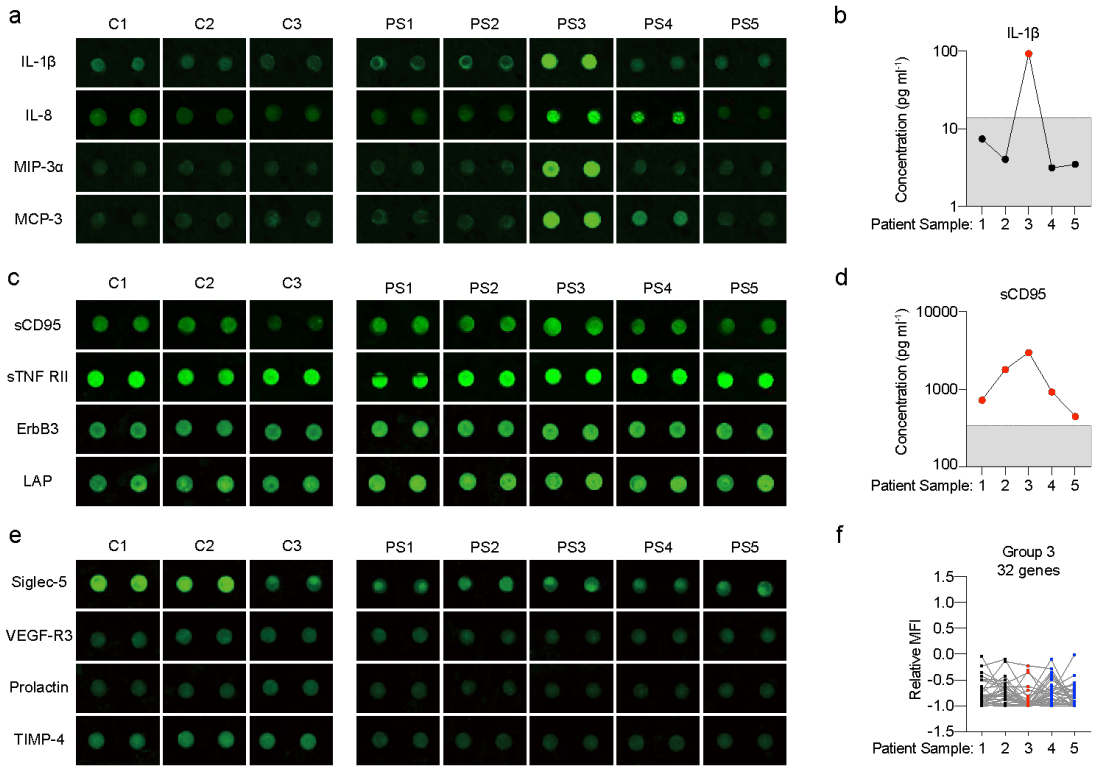

868

869 **Extended Data Fig. 4** | Cytokine array analysis of patient's serum.

870 Images of representative cytokines in group 1 (**a**), group 2 (**c**) and group 3 (**e-f**) clustered from cytokine

871 array data according to Fig. 2l-n were presented. Typical cytokines were re-validated with ELISA (**b, d**)

872 and integrated relative MFI plots of group 3 cytokines were shown.

873

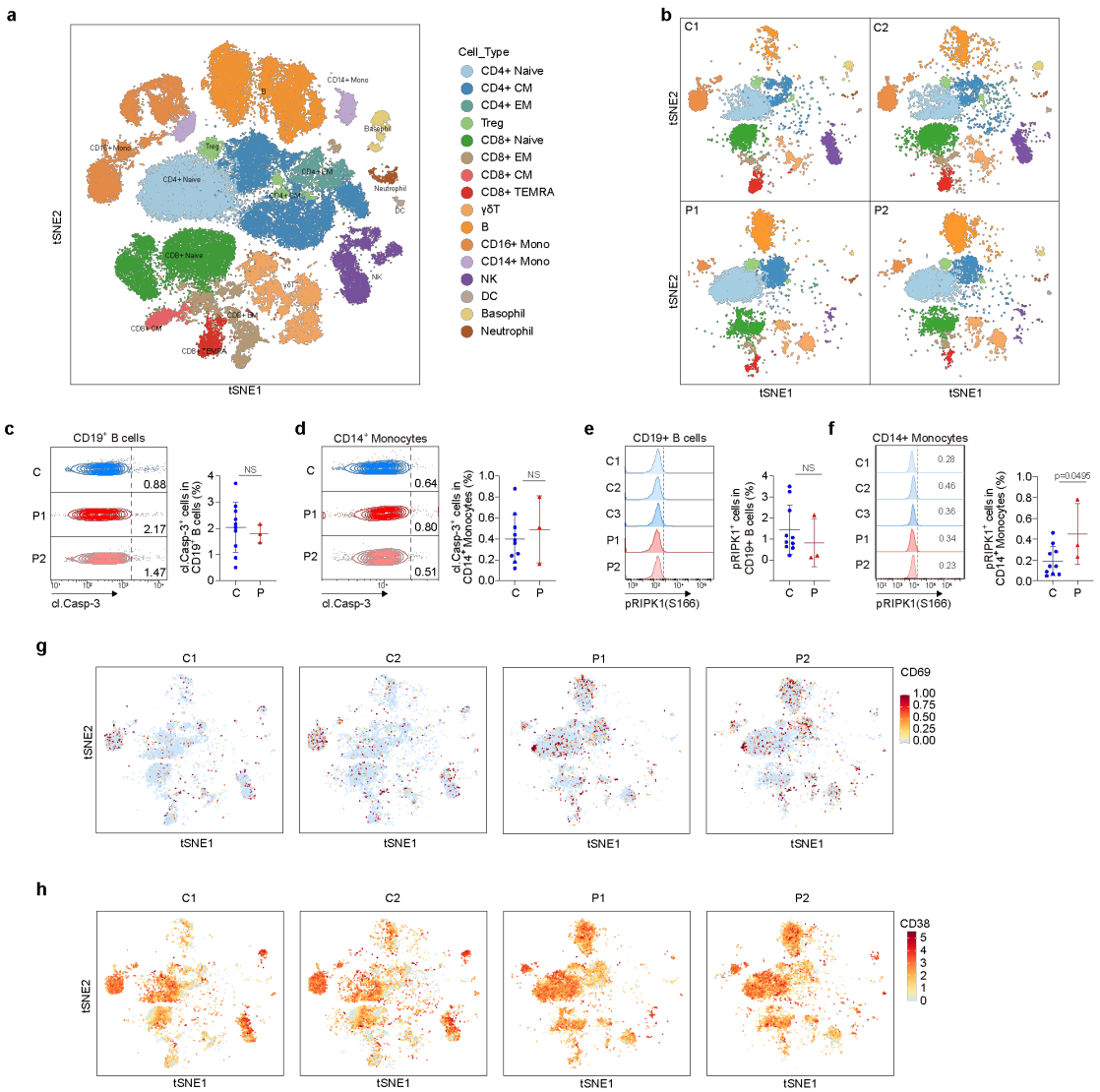

874

875 **Extended Data Fig. 5** | CyTOF profiling of patients' PBMCs.

876 **a-b,** Integrated t-distributed stochastic neighbor embedding (tSNE) visualization of CyTOF
877 immunophenotyping of PBMCs from four unaffected controls and two patients (**a**). Major 16 cell
878 lineages from all samples were identified through unsupervised clustering with FlowSOM. tSNE plots
879 showing 10000 cells of representative C1, C2, P1 and P2 with color-indicated cell types (**b**). **c-f,**
880 Representative contour plots of cl. Casp-3 (**c-d**) and histograms of pRIPK1(S166) (**e-f**) protein levels in
881 $CD19^+$ B cells and $CD14^+$ monocytes in freshly isolated PBMCs from unaffected controls (n=10) and
882 patients (n=3 for P1 and P2) (left panel). Summary histograms were shown with mean±SD (right panel).
883 **g-h,** t-distributed stochastic neighbor embedding (tSNE) plot showing the CD69 and CD38 expression
884 in CyTOF analysis. Statistical significance was determined by two-tailed unpaired t-test. ns, $P > 0.05$,
885 $*P<0.05$, $**P < 0.01$, $***P < 0.001$.

886

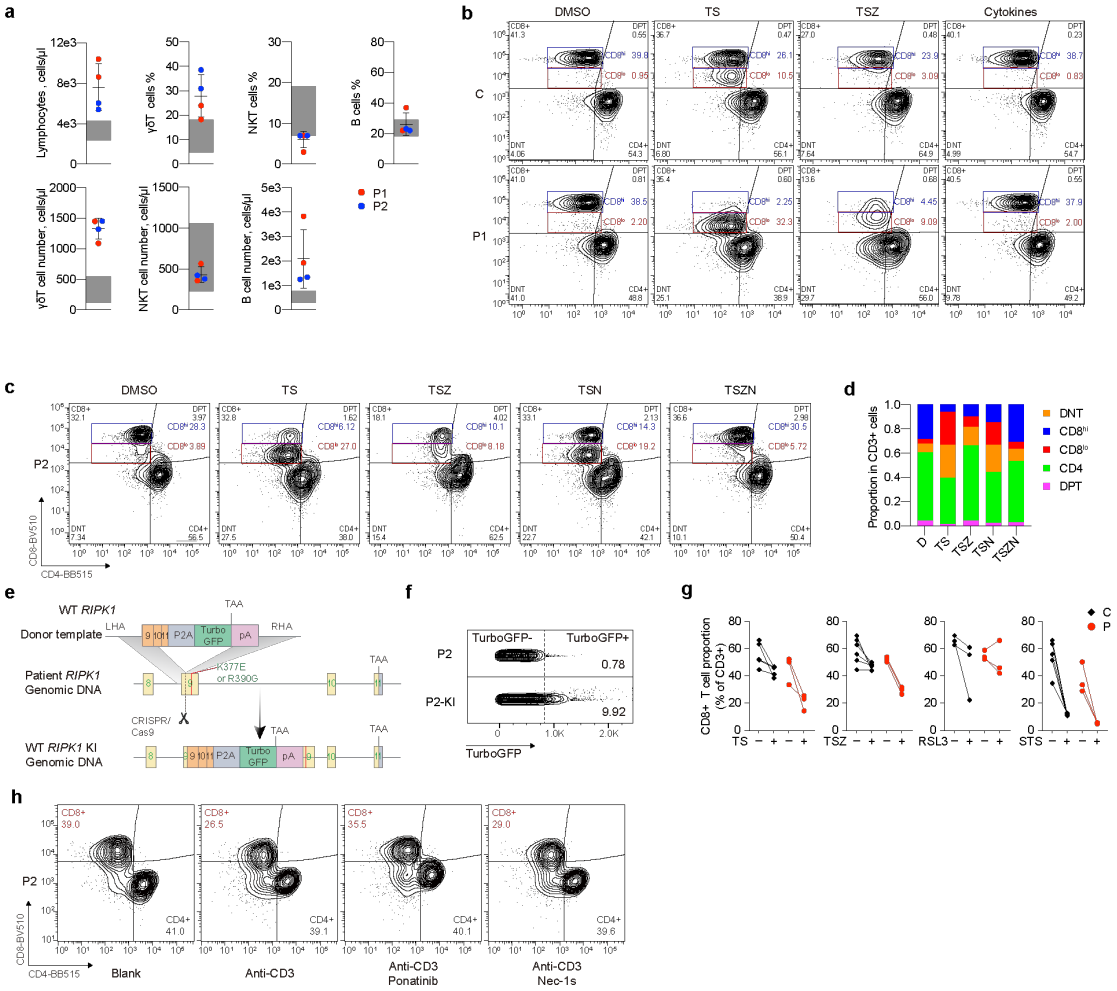

Extended Data Fig.6 | RIPK1-mediated cell death leads to CD8 decrease in T cells.

a, Percentages and absolute counts of total lymphocytes, γδ T cells, NKT cells and B cells from whole blood of P1 (red dots) and P2 (blue dots) measured by immunophenotyping. **b,** Representative contour plots showing percentages of CD8^{hi} T, CD8^{lo} T, CD4^{+} T, DNT and DPT cells in CD3^{+} T cells isolated from unaffected control and P1 under the stimulation of TS, TSZ and cytokines (combination of IL-1β (10 ng ml^{-1}), IL-6 (100 ng ml^{-1}), IFNα (100 ng ml^{-1}) and IL-8 (100 ng ml^{-1})) as indicated for 6 hours. **c-d,** Representative contour plots (**c**) and summary histogram (**d**) showing percentages of CD8^{hi} T, CD8^{lo} T, CD4^{+} T, DNT and DPT cells in CD3^{+} T cells isolated from P2 under the stimulation of TS, TSZ, TSN and TSZN as indicated for 6 hours. **e,** Schematic of CRISPR/Cas9-mediated *in situ* knock-in of WT *RIPK1* into patients' *RIPK1* locus. **f,** Representative contour plots of Turbo-GFP^{+} cells percentage indicating WT *RIPK1* knockin efficiency. **g,** Statistical analysis of CD8^{+} T cell proportions in CD3^{+} T cells from unaffected controls (n=3-6) and two patients (n=3 for P1 and P2) under the stimulation of TS, TSZ as well as RSL3 (1 µM) and STS (100 nM) for indicated times. **h,** Representative contour plots showing percentages of CD8^{+} T and CD4^{+} T cells in CD3^{+} T cells isolated from P2 under the stimulation

902 of anti-CD3 antibody (5 μg/ml) with or without Ponatinib (250 nM) and Nec-1s (10 μM) for 24 hours. T
903 denotes 20 ng ml^{-1} TNF; S denotes 250 nM SM-164; Z denotes 25 μM z-VAD-fmk; N denotes 10 μM
904 Nec-1s. Graphs show mean±SD.
905

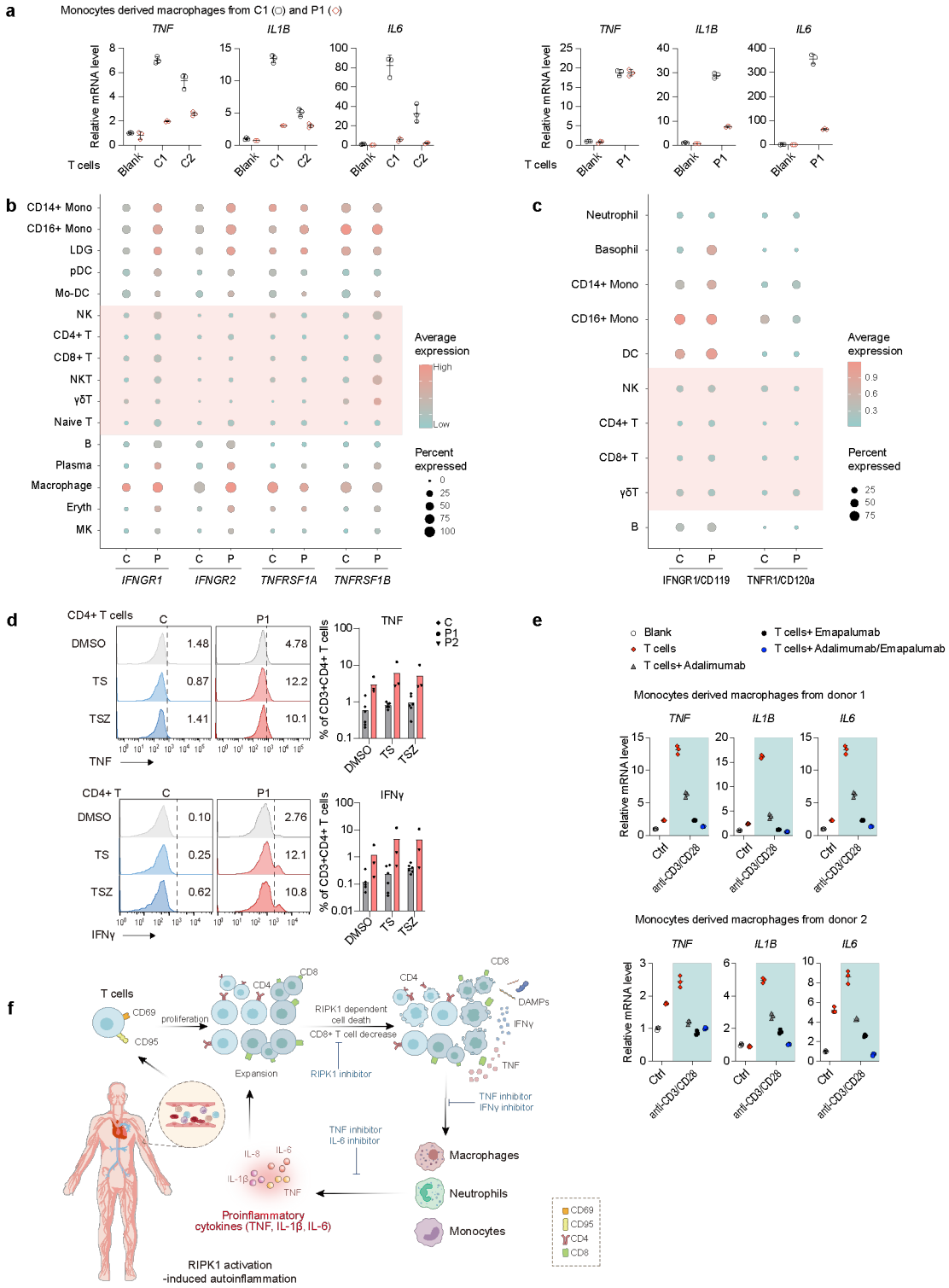

Extended Data Fig. 7 | TNF/IFNγ links T-mono axis.

a, qRT-PCR analysis of *TNF, IL1B* and *IL6* mRNA levels in GM-CSF-activated monocytes derived macrophages (MDMs) co-cultured with or without T cells for 6 hours. GM-CSF activated MDMs

generated from C1 (blank dots) or P1 (red dots) were co-cultured with T cells from unaffected controls (C1 and C2, left panel) or P1 (right panel) as indicated. **b-c,** Dot plot showing the mRNA expression of *IFNGR1*, *IFNGR2*, *TNFRSF1A* and *TNFRSF1B* from sc-RNAseq analysis (**b**) or protein levels of IFNGR1/CD119 and TNFR1/CD120a from CyTOF analysis (**c**) in cell subtypes found in PBMCs. The size of the circle indicates the percentages of cells positive for gene expression and the color represents the average expression levels. **d,** Representative histograms and statistical analysis of TNF and IFNγ expression in $CD4^+$ T cells in PBMCs isolated from unaffected controls (n=6) and patients (n=3 for P1 and P2) treated with TS and TSZ for 24 hours. **e,** T cells stimulated with or without anti-CD3/CD28 dynabeads for 24 hours prior to co-culture with MDMs generated from healthy donor 1 (upper panel) or donor 2 (bottom panel) in the presence of 10 μg ml^{-1} adalimumab, 10 μg ml^{-1} emapalumab alone or in combination for 6 hours. *TNF, IL1B* and *IL6* mRNA levels of MDMs were analyzed by qRT-PCR. **f,** Working model: RIPK1 activation-dependent $CD8^+$ T cell death-triggered inflammatory response of myeloid cells cause SAID. Dots represent each image and graphs show mean±SD.

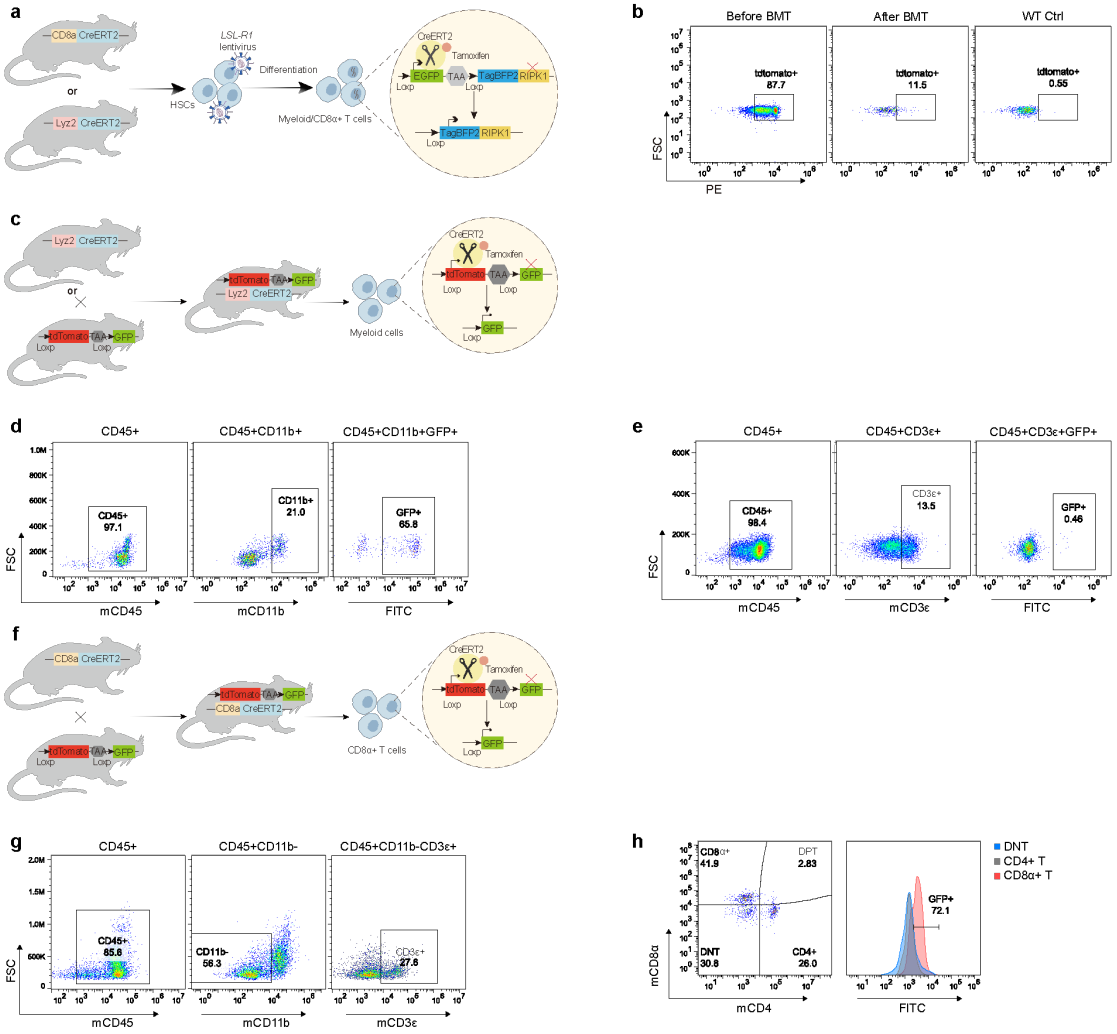

Extended Data Fig. 8 | Specificity and efficiency of conditional expression system.

a, Schematic representation depicting conditional human RIPK1 overexpression system in murine HSC used in this study. **b,** Representative contour plots showing the bone marrow transplantation efficiency. **c-h,** Schematic representation depicting the generation of double transgenic mice used to evaluate the specificity and efficiency of *Lyz2*-CreERT2 (**c**) and *Cd8a*-CreERT2 (**f**). Representative contour plots showing percentage of GFP^{+} cells in myeloid (**d**) and T lymphoid lineage(**e**), as well as in T cell subsets (**g, h**) from the whole blood of *Lyz2*-CreERT2::*Rosa26*-mTmG and *Cd8a*::*Rosa26*-mTmG mice with tamoxifen induction.

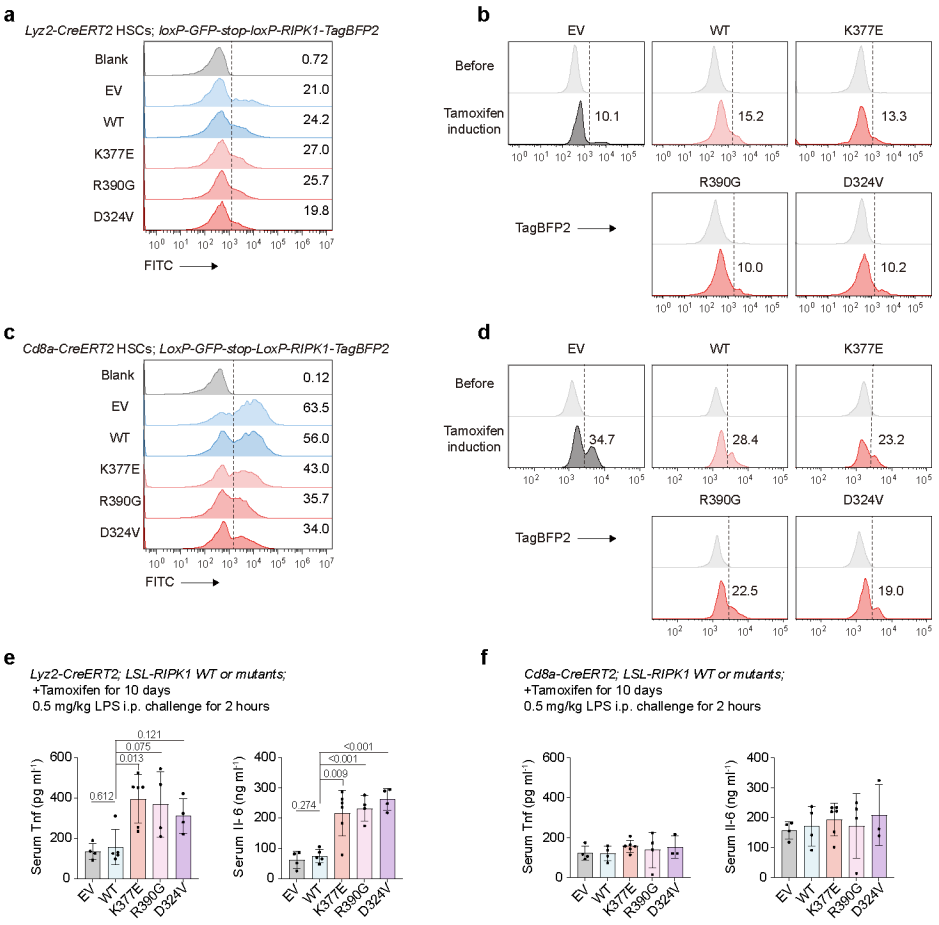

Extended Data Fig. 9 | Efficiency of conditionally induced overexpression of RIPK1 in mice. **a-d,** *loxp-GFP-stop-loxp-TagBFP2-P2A-WT/mutated human RIPK1* were lentivirally transduced into HSCs isolated from *Lyz2*-CreERT2 (**a**) or *Cd8a*-CreERT2 donor mice (**c**). Histogram graphs showing expression levels of GFP in HSCs. Whole blood cells isolated from recipient mice with *Lyz2*-CreERT2 (**b**) and *Cd8a*-CreERT2 (**d**) HSCs transplantation before and after tamoxifen induction. Histogram graphs showing expression levels of TagBFP2 in myeloid cells (**b**) and CD8α$^+$ T cells (**d**). **e-f,** ELISA measurement of serum Tnf and Il-6 levels in mice specifically overexpressing WT or mutated hRIPK1 in myeloid cells (**e**) or CD8α$^+$ T cells (**f**) with 0.5 mg/kg LPS challenge for 2 hours. Statistical significance was determined by two-tailed unpaired t-test.

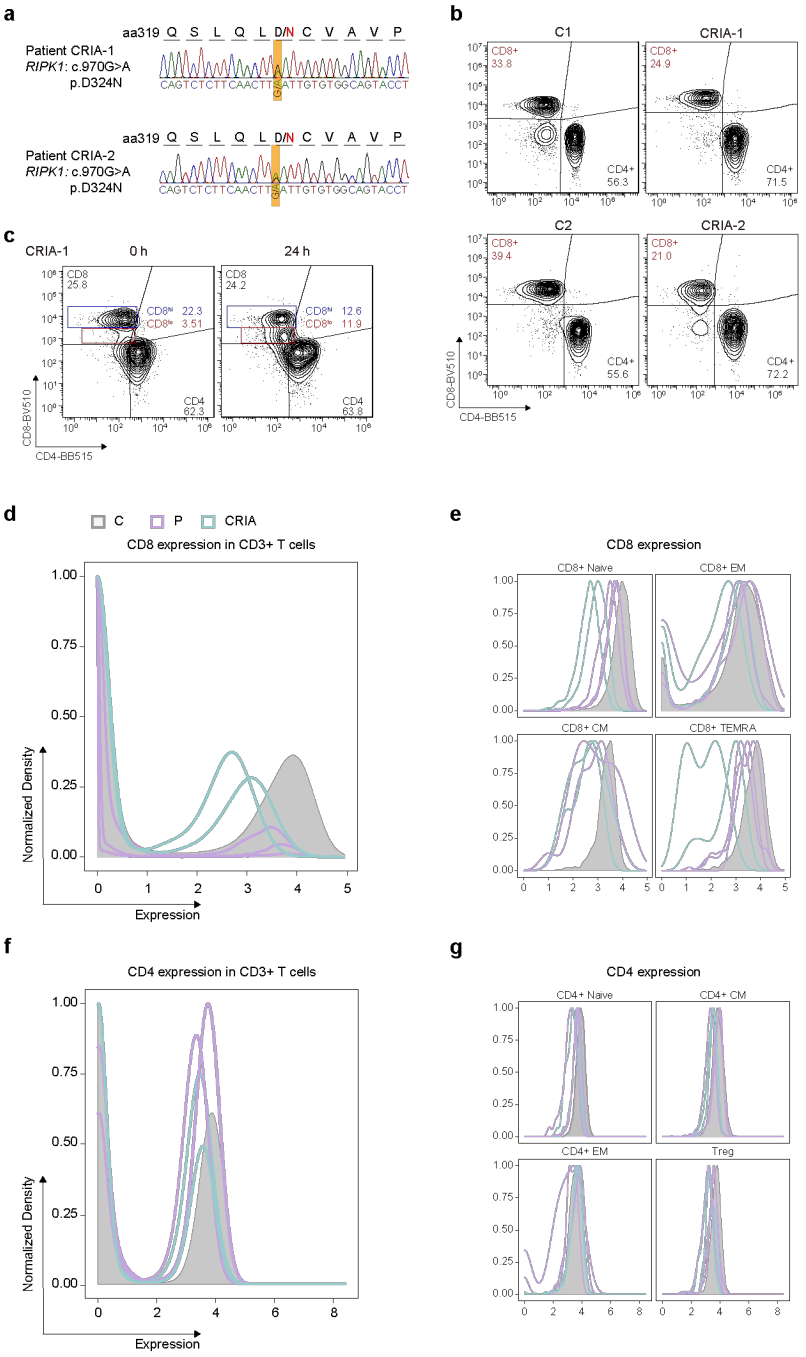

Extended Data Fig. 10 | CD8 expression in CRIA patients.

a, Sanger sequencing chromatograms of *RIPK1* in whole blood genomic DNA from CRIA patients (CRIA-1 and CRIA-2). **b**, Representative contour plots showing percentages of $CD4^+$ T and $CD8^+$ T cells in $CD3^+$ T cells isolated from CRIA patients. **c,** Representative contour plots depicting the percentages of $CD4^+$ T, $CD8^+$ T, double negative T (DNT) and double positive T (DPT) in $CD3^+$ T cells gated from PBMCs of CRIA-1 culturing *in vitro* for 24 hours. **d-g,** Contour plots showing the expression of CD8 (**d**) or CD4 (**f**) in $CD3^+$ T cells, $CD8^+$ (**e**) and $CD4^+$ (**g**) T cell subsets of four unaffected controls, two patients (P1 and P2) and two CRIA patients. The protein expression was determined using CyTOF.